Revisiting the Middle Eocene Climatic Optimum 'Carbon Cycle Conundrum' with new estimates of atmospheric pCO2 from boron isotopes

Henehan, Michael; Edgar, Kirsty; Foster, Gavin L.; Penman, Donald; Hull, Pincelli; Greenop, Roseanna; Anagnostou, Eleni; Pearson, Paul N.

DOI:
10.1029/2019PA003713

Document Version
Peer reviewed version

Citation for published version (Harvard):
Henehan, M, Edgar, K, Foster, GL, Penman, D, Hull, P, Greenop, R, Anagnostou, E & Pearson, PN 2020, 'Revisiting the Middle Eocene Climatic Optimum 'Carbon Cycle Conundrum' with new estimates of atmospheric pCO_2 from boron isotopes', *Paleoceanography and Paleoclimatology*. https://doi.org/10.1029/2019PA003713

Revisiting the Middle Eocene Climatic Optimum 'Carbon Cycle Conundrum' with new estimates of atmospheric pCO_2 from boron isotopes

Michael J. Henehan[1,2,3*], Kirsty M. Edgar[4*], Gavin L. Foster[1], Donald E. Penman[3], Pincelli M. Hull[3], Rosanna Greenop[5], Eleni Anagnostou[6] and Paul N. Pearson[7].

[1]*School of Ocean and Earth Science, National Oceanography Centre Southampton, University of Southampton, SO14 3ZH, UK*
[2]*GFZ German Research Centre for Geosciences, Telegrafenberg, 14473 Potsdam, Germany.*
[3]*Department of Geology & Geophysics, Yale University, PO 208109, New Haven, CT, 06520-8109, USA*
[4]*School of Geography, Earth and Environmental Sciences, University of Birmingham, B15 2TT, UK*
[5]*Department of Earth Sciences, Irvine Building, University of St. Andrews, St. Andrews KY16 9AL, Scotland, UK*
[6]*GEOMAR Helmholtz Center for Ocean Research Kiel, 24148 Germany*
[7]*School of Earth and Ocean Sciences, Cardiff University, Cardiff, CF10 3AT, UK*

(Correspondence to: Michael.Henehan@gfz-potsdam.de; ORCID: 0000-0003-4706-1233)

Key Points:

- We present a new record of pCO_2 across the MECO, from boron isotopes in foraminifera from multiple ocean drilling sites.
- Incorporating carbon cycle modelling, our data indicate pCO_2 rise of about two thirds of a doubling across the event.
- pCO_2 change during the MECO onset warming was limited, indicating heightened climate sensitivity or a non-thermal component to $\delta^{18}O$ change.

Abstract

The Middle Eocene Climatic Optimum (MECO) was a gradual warming event and carbon cycle perturbation that occurred between 40.5 and 40.1 Ma. A number of characteristics, including greater-than-expected deep-sea carbonate dissolution, a lack of globally-coherent negative $\delta^{13}C$ excursion in marine carbonates, a duration longer than the characteristic timescale of carbon-cycle recovery, and the absence of a clear trigger mechanism, challenge our current understanding of the Earth system and its regulatory feedbacks. This makes the MECO one of the most enigmatic events in the Cenozoic, dubbed a middle Eocene 'carbon cycle conundrum'. Here we use boron isotopes in planktic foraminifera to better constrain pCO_2 changes over the event. Over the MECO itself, we find that pCO_2 rose by only 0.55-0.75 doublings, thus requiring a much more modest carbon injection than previously indicated by the alkenone $\delta^{13}C$-pCO_2 proxy. In addition, this rise in pCO_2 was focused around the peak of the 400 kyr warming trend. Before this, considerable global carbonate $\delta^{18}O$ change was asynchronous with any coherent ocean pH (and hence pCO_2) excursion. This finding suggests that middle Eocene climate (and perhaps a nascent cryosphere) was highly sensitive to small changes in radiative forcing.

Plain Language Summary

Geoscientists often look to periods of global warming in the geological past to understand how the Earth responds to input of atmospheric CO_2. However, during the Middle Eocene Climatic Optimum (or MECO) 40 million years ago, the Earth did not respond in the way one would expect, given what we know from these earlier warming events. The MECO poses a number of puzzles for geoscientists relating to what caused it, and why the Earth system responded in the way it did. Before we can hope to answer these questions, however, we need to know what atmospheric CO_2 levels were in the middle Eocene, and how much they changed over the MECO event. Here we use boron isotope ratios in fossil plankton shells to tell us how ocean pH (which predominantly reflects CO_2 levels) changed over the MECO. We show that relatively little change in CO_2 at this time were associated with large-scale changes in climate. This suggests that during the Eocene, when CO_2 levels were similar to those likely to be reached by the end of this century, the Earth's climate (and possibly ice sheets) were very sensitive to minor disturbances.

1. Introduction

The Middle Eocene Climatic Optimum (MECO; ~ 40.1 – 40.5 Ma) was a global warming event during which marine bulk and benthic carbonate $\delta^{18}O$ values steadily declined by roughly 1 ‰ in over ~400 kyr, usually interpreted as 3-6 ˚C of global temperature rise (Bohaty et al., 2009; Bohaty & Zachos, 2003). While sometimes referred to as a hyperthermal event (e.g. Arreguín-Rodríguez et al., 2016; Pomar et al., 2017), the MECO differs fundamentally from the true hyperthermal events earlier in the Paleogene, such as the Paleocene-Eocene Thermal Maximum (PETM, ~56 Ma) or Eocene Thermal Maximum 2 (ETM2; ~53.7 Ma). Firstly, these hyperthermal events were rapid in their onset (< 10 kyr; Kirtland Turner et al., 2017) and were followed by a gradual return to roughly pre-event temperatures as the silicate weathering feedback drew down atmospheric CO_2 (e.g. Kelly et al., 2005; Penman, 2016; Penman et al., 2016; Zachos et al., 2005), whereas the MECO saw a steady decline in carbonate $\delta^{18}O$ values over several 100 kyr (interpreted as gradual warming), followed by a rapid return to pre-event conditions (Bohaty et al., 2009). A second important distinction is that the earlier hyperthermal events are clearly marked by sharp drops in $\delta^{13}C$ that are expressed globally in both marine $CaCO_3$ and terrestrial records (e.g. Abels et al., 2012; Kennett & Stott, 1991; Koch et al., 1992; Westerhold et al., 2018; Zachos et al., 2005). These carbon isotope excursions (or CIEs) are thought to be manifestations of rapid injections of isotopically light C into the Earth system, perhaps from volcanic sills intruding into organic rich sediments (Gutjahr et al., 2017; Storey et al., 2007; Svensen et al., 2004) and/or the release of seafloor methane clathrates (Dickens et al., 1995). A small negative $\delta^{13}C$ excursion is observed at the peak of the 400 kyr MECO warming trend in most marine records, but is not uniformly expressed (e.g. at ODP Site 1263; Bohaty et al., 2009) and appears in some cases to lag behind minimum $\delta^{18}O$ values (e.g. at ODP Site 702; Bohaty et al., 2009). Furthermore, during the first few 100 kyr of warming, patterns of carbon isotope change are inconsistent between sites: global bulk carbonate $\delta^{13}C$ values display inverse trends in each hemisphere, with progressively lighter $\delta^{13}C$ during MECO warming in northern latitudes, minimal $\delta^{13}C$ change in the tropics, and progressively heavier $\delta^{13}C$ during warming towards the southern high latitudes (Bohaty et al., 2009). Thus, unlike the hyperthermal events, the MECO is difficult to attribute to a simple, rapid injection of exogenous isotopically-light carbon.

One characteristic that the MECO perhaps unexpectedly shares with the hyperthermal events is extensive dissolution of deep-sea sediments, representing a shoaling of the carbonate compensation depth (CCD; Bohaty et al., 2009; Bohaty & Zachos, 2003). During the hyperthermal events, this carbonate dissolution occurred in response to CO_2 being injected into the ocean-atmosphere system faster than the capacity of silicate weathering on land to draw it down and input alkalinity to the ocean (see e.g. Berner et al., 1983; Colbourn et al., 2015; Kirtland Turner et al., 2017). MECO warming, however, was nearly an order of magnitude slower than the PETM, and as such chemical weathering feedbacks should have kept pace with warming (Colbourn et al., 2015; Sluijs et al., 2013). This would be expected to have driven a deepening of the CCD instead of the ~1 km shoaling observed. Moreover, at the MECO there is little signal of a 'carbonate overshoot' following the event (Bohaty et al., 2009; Sluijs et al., 2013), as is seen after the PETM (Penman et al., 2016). Since these carbonate overshoots are thought to reflect the Earth's silicate weathering feedback drawing down injected CO_2, the absence of any such event after the MECO might suggest either a) a relatively small addition of CO_2, and/or b) a weakened silicate weathering response to CO_2 rise during this interval. The latter scenario is favored by a recent study by van der Ploeg et al. (2018), who observed a reduction in the $^{187}Os/^{188}Os$ composition of seawater over the MECO. While this observation could be consistent with either i) a rise in hydrothermal activity, ii) an increase in weathering of mafic silicate rocks, or iii) a decrease in weathering of felsic radiogenic continental rocks, a reduction in continental weathering is more easily reconciled with deep sea carbonate dissolution. Consequently, van der Ploeg et al. hypothesize that after tens of millions of years of intense weathering under greenhouse Eocene climates, Earth's silicate weathering feedback was no longer strong enough to buffer a carbon cycle imbalance at the MECO (van der Ploeg et al., 2018).

While a weakened silicate weathering feedback is an intriguing hypothesis, it does pose its own questions. Firstly, the idea that the baseline middle Eocene earth surface was no longer as readily weatherable is based on Li isotopes measured in foraminifera (Misra & Froelich, 2012). However, even leaving potential non-seawater controls on foraminiferal δ^7Li aside (Roberts et al., 2018; Vigier et al., 2015), there is more than one possible solution that could have resulted in light seawater δ^7Li, including sustained high rates of regolith chemical weathering and soil production (Vigier & Goddéris,

2015). Secondly, one of the most pronounced features of the MECO is a rapid (10s of kyr) drop in temperatures after the peak of the warming trend, which would indicate some unexplained reactivation of the silicate weathering feedback after million years of hypothesized gradual decline.

Another outstanding question surrounding the MECO is that of causality. The long, drawn-out nature of the MECO warming might suggest a sustained CO_2 release, and hence perhaps a volcanic source, by analogy to the several 100 kyr-long late Maastrichtian warming event (LMWE) thought to have been caused by Deccan outgassing (e.g. Barnet et al., 2018; Henehan, Hull, et al., 2016). A number of potential sources of volcanic CO_2 at the MECO exist (summarized in van der Ploeg et al., 2018), but the synchronicity of any one volcanic degassing event with MECO warming is yet to be demonstrated. Besides this, the coincidence of the MECO with a 2.4 Myr very long eccentricity cycle minimum (Westerhold & Röhl, 2013) might implicate an orbital trigger instead. These long eccentricity 2.4 Myr cycles have recently been shown to coincide with numerous excursions in $\delta^{13}C$ and $\delta^{18}O$ during the early Cenozoic (Barnet et al., 2019; Kocken et al., 2019), and carbon cycle models have been able to reproduce significant changes in the Earth's carbon cycle due to oscillating carbon reservoirs on these timescales, inducing sizeable changes in pCO_2 and the CCD (Kocken et al., 2019). Observed cyclical changes in the Pacific CCD in the Eocene (Lyle et al., 2005; Pälike et al., 2012) appear to have a roughly 2.4 Myr periodicity (Kocken et al., 2019), and the MECO follows the most pronounced and extreme of these periodic carbonate accumulation events (CAEs) (Lyle et al., 2005). It is possible that a combination of volcanic outgassing and a favorable orbital configuration may have been key to the amplification of the MECO as a major carbon cycle perturbation, as has been suggested for the PETM and LMWE (Barnet et al., 2019). Alternatively, it is also conceivable that orbital configuration alone could have independently induced carbon cycle changes (as with the Early-Late Paleocene Event; Barnet et al., 2019), perhaps through changing rainfall patterns and hence silicate weathering intensity (Westerhold & Röhl, 2013). Indeed, repeating patterns in carbonate $\delta^{13}C$ and $\delta^{18}O$ values (Fig. 1) might favor some such internally-modulated, pseudo-cyclic carbon cycle imbalance rather than a stochastic carbon injection from a volcanic source.

Constraining atmospheric pCO_2 across the MECO is central to understanding both the causal drivers of the MECO and the Earth system's enigmatic response to the event. The only published

155 pCO_2 reconstruction over the MECO to date is that of Bijl et al. (2010), derived from alkenone $\delta^{13}C$.
156 While undoubtedly pioneering, the record poses even more questions of its own, in that taken at face
157 value it indicates several high-amplitude fluctuations on the order of several thousand µatm of CO_2
158 over the MECO, asynchronous with a near-linear decline in $\delta^{18}O$. This would appear incongruous in
159 the context of background pCO_2 levels in the middle Eocene reconstructed from boron isotopes
160 (Anagnostou et al., 2016), and would require extremely large masses of carbon to have been injected
161 into - and subsequently removed from - the Earth system on geologically short timescales with no
162 discernible influence on carbonate $\delta^{13}C$ values. Here, we revisit this issue using the boron isotope
163 ($\delta^{11}B$) pH proxy (see e.g. Foster & Rae, 2016; Hemming & Hanson, 1992) to generate new,
164 independent estimates of ocean pH and pCO_2 change at this time. We then explore the significance of
165 our record in constraining causal mechanisms, global weathering feedbacks and climate sensitivity
166 over this enigmatic event.
167
168 ## 2. Materials and Methods
169 ### 2.1. Site and Species Selection
170 We analyzed single-species mixed-layer foraminifera primarily at the equatorial Pacific ODP
171 Site 865 (1300-1500 m paleo-depth (Bralower et al., 1995)), which has been the subject of previous
172 boron isotope investigations (Edgar et al., 2015; Pearson & Palmer, 1999, 2000). To ascertain to what
173 extent our resultant pCO_2 record was globally representative, we compared these data with lower-
174 resolution measurements from three other deep-sea drill sites, spanning a wide range of oceanographic
175 settings (Fig. 2): ODP Sites 1260 (equatorial Atlantic; ~2,500-3,200 m paleo-depth (Sexton, Wilson,
176 & Norris, 2006; Shipboard Scientific Party, 2004a)), 1263 (mid-latitude South Atlantic; ~2000 m
177 paleo-depth (Shipboard Scientific Party, 2004b)) and 702 (Southern Ocean; ~2250 m paleo-depth
178 (Katz & Miller, 1991; Shipboard Scientific Party, 1988)). High-resolution bulk carbonate or benthic
179 foraminiferal $\delta^{13}C$ and $\delta^{18}O$ stratigraphies are available for each site (Bohaty et al., 2009; Boscolo
180 Galazzo et al., 2014; Edgar et al., (in prep.), 2010; Sexton, Wilson, & Pearson, 2006b), allowing cross-
181 correlation. All sites are open-ocean in setting and remain above the local CCD across the event,
182 although at ODP Site 1260 multiple clay layers are evident within the MECO (Edgar et al., 2010),

indicating that this site was close to the local lysocline. It is likely, therefore, that our sampling at ODP Site 1260 misses the peak of the MECO event. Calcareous nannofossil and foraminiferal communities from ODP Sites 865 indicate that sediments were deposited under oligotrophic open-ocean conditions (Bralower et al., 1995) suggesting that $[CO_2]_{aq}$ reconstructed at these sites was likely in (near) equilibrium with the atmosphere with respect to CO_2. Abundant siliceous microfossils suggest more productive surface ocean conditions at ODP Sites 1260 and 702, while productivity at ODP Site 1263 appears to vary temporally over the event (Boscolo Galazzo et al., 2015).

At each site, mono-specific separates (136-343 tests, 1.8-4.3 mg $CaCO_3$) of planktic foraminifera were picked for $\delta^{11}B$ analyses from the 250-300 μm sieve size range to minimize any ontogenetic or metabolic effects. We selected the shallowest-dwelling foraminiferal species possible at each site, given the sample size requirements for analysis. Specifically, these were *Globigerinatheka index* (at ODP Site 702*)*; *Acarinina praetopilensis* (ODP Site 865); *Morozovelloides crassatus* (ODP Site 1260); and *Globigerinatheka kugleri* (ODP Site 1263). Foraminifera at all sites are recrystallized, but the degree of diagenetic recrystallization varies between sites (see Sr/Ca data, Supplementary Data). The most pervasive alteration is seen at ODP Site 865, but even extensive recrystallization in Eocene sediments from this site appears to have had little influence on fossil foraminiferal $\delta^{11}B$ values (Edgar et al., 2015).

2.2 Age models

All ages are reported on the Geological Timescale 2012 (Gradstein et al., 2012). Sites were aligned using a combination of stable isotopic, magneto- and bio- stratigraphic tie-points. An internally-consistent age model for all sites was constructed based on ODP Site 702, which has the most complete magnetostratigraphy (Clement & Hailwood, 1991) and most highly resolved bulk stable isotope stratigraphy in this study (Bohaty et al., 2009). All stable isotope tie-points were calibrated at this site based on linear interpolation between magnetochron boundaries. Although magnetostratigraphy at all sites was developed with biostratigraphic controls in mind, we used bioevent tie-points for age control only outside of the focal interval, at depths where no stable isotope stratigraphy or reliable magnetic datums were available for correlation. This is because bioevents are

difficult to employ for correlation across such a large latitudinal range used in this study, given likely faunal differences between sites at any one time. Immediately surrounding and within the MECO itself, stable isotope tie-points were most useful for correlation. Our age models therefore represent a compromise between number of robust (easy-to-pick) tie points and alignment of major stable isotope features at all sites. A full list of the stable isotope tie-points used in this study and the age assigned to each are shown in Table S1, and are plotted in the depth domain in Fig. S1.

2.3 Analytical methods

Boron isotope analyses were carried out on a Thermo Neptune Multi-Collector ICP-MS at the University of Southampton following Foster (2008). External reproducibility is estimated from ^{11}B signal intensity (primarily dictated by sample size) using a relationship between intensity and long-term reproducibility at the University of Southampton from Greenop et al. (2017). Sample cleaning and preparation follows established protocols (see Anagnostou et al., 2016; Henehan, Foster, et al., 2016 and references therein). For each sample, a subsample of cleaned, crushed foraminiferal carbonate was taken for $\delta^{13}C$ and $\delta^{18}O$ analysis, while an aliquot of dissolved material was taken prior to boron column chemistry for trace and minor element analysis (B, Mg, Al, Sr). Trace element analysis was carried out using a Thermo Element ICP-MS at the University of Southampton. Long-term reproducibility (2 sd) was ±< 5% for Al/Ca ratios measurements, and ±< 3% for Mg/Ca and Sr/Ca. Al/Ca ratios for samples analysed here are all < 105 µmol/mol; below an operational threshold of ~140 µmol/mol commonly used to indicate clay contamination (Rae et al., 2011). Foraminiferal $\delta^{13}C$ and $\delta^{18}O$ analyses from ODP Sites 702, 865, 1260 and 1263, were made on a Thermo Scientific Delta V Advantage mass spectrometer coupled to a GasBench II at Cardiff University and are reported relative to the Vienna Pee Dee Belemnite (VPDB) standard with an external analytical precision (1σ) of 0.06 ‰ for $\delta^{13}C$ and 0.07 ‰ for $\delta^{18}O$. Further samples from IODP Site U1408 were measured for $\delta^{13}C$ and $\delta^{18}O$ on a Thermo Kiel IV coupled to a Thermo MAT 253 mass spectrometer at Yale University, with typical external precision (1σ) of <0.03‰ for $\delta^{13}C$ and <0.04‰ for $\delta^{18}O$ based on replicate analyses of in-house (TS, MERC, CM, PX) and international (NBS19) standards.

2.4 Vital effects

To calculate ocean pH from foraminiferal $\delta^{11}B$ values, one must first consider the possible influence of 'vital effects'. Photosynthetic activity of symbiotic algae elevates seawater pH in the immediate microenvironment around host planktic foraminifera, while symbiont and host respiration lowers pH (see e.g. Henehan, Foster, et al., 2016; Hönisch et al., 2003; Jørgensen et al., 1985; Köhler-Rink & Kühl, 2005; Zeebe et al., 2003). Because of varying rates of photosynthesis and respiration, foraminiferal species living in similar ambient seawater pH may record different $\delta^{11}B$ values (see e.g. Anagnostou et al., 2016; Henehan, Foster, et al., 2016; Hönisch et al., 2003). While almost all studied modern planktic foraminifera record $\delta^{11}B$ values offset from ambient $\delta^{11}B_{borate}$ (Anagnostou et al., 2016; Henehan, Foster, et al., 2016 and references therein), recent work has suggested that vital effects were dampened in the Eocene relative to today (Anagnostou et al., 2016) and as such, further investigation was necessary.

Vital effects in extinct species can be gauged by comparison of $\delta^{11}B$, $\delta^{13}C$, $\delta^{18}O$ and B/Ca ratios across a foraminiferal assemblage (Anagnostou et al., 2016; Edgar et al., 2015; Henehan, Foster, et al., 2016) and/or using intra-specific body size-$\delta^{13}C$ and $\delta^{18}O$ gradients (Birch et al., 2012; D'Hondt et al., 1994; Edgar et al., 2013; Ezard et al., 2015; Pearson et al., 1993; Sexton, Wilson, & Pearson, 2006b). To constrain vital effects in the species measured here, we made new $\delta^{13}C$ and $\delta^{18}O$ measurements of well-preserved "glassy" foraminifera from IODP Site U1408 where all of the species measured here co-existed in a single time-slice (Norris et al., 2014) (Fig. 3). This new $\delta^{13}C$ and $\delta^{18}O$ data support a shallow mixed-layer habitat for *A. praetopilensis and M. crassatus*. However, our data support a somewhat deeper mixed-layer habitat for *G. index* and *G. kugleri*, as suggested elsewhere (Anagnostou et al., 2016; Edgar et al., 2013, 2015; Pearson et al., 1993, 2001, 2006; Sexton, Wilson, & Pearson, 2006b). Globigerinathekids record cooler $\delta^{18}O$-temperatures than *M. crassatus* and *A. praetopilensis* (Fig. 3a), with *G. index* in particular indicating progressively deeper habitat in size fractions larger than those analysed here, perhaps reflecting the addition of gametogenic crusts at depth (Pearson et al., 1993; Premoli Silva et al., 2006; Sexton, Wilson, & Pearson, 2006b). With regards $\delta^{13}C$, globigerinathekids at Site U1408 record lower values than *M. crassatus* or *A. praetopilensis*, indicating weaker photosynthetic activity in their microenvironment and/or a deeper mean habitat. Whilst *G. kugleri* displays a strong positive $\delta^{13}C$ gradient with increasing size (Fig. 3b)

consistent with symbiont-bearing foraminifera (Ezard et al., 2015; Pearson et al., 1993; Spero et al., 1991), *G. index* does not, suggesting high latitude *G. index* had few or no photosynthetic symbionts. Thus, our focal species likely have varying degrees of influence from photosymbionts. By analogy with extant taxa, these species are expected to display variable offsets from aqueous $\delta^{11}B_{borate}$ (Henehan, Foster, et al., 2016). We therefore assign calibrations by analogy with modern taxa based on our $\delta^{13}C$ and $\delta^{18}O$ data, and published observations (Anagnostou et al., 2016; Edgar et al., 2013; Pearson et al., 1993, 2001; Sexton, Wilson, & Pearson, 2006b). For *A. praetopilensis* and *M. crassatus* we apply a calibration based on the low-latitude, mixed layer-dwelling, dinoflagellate-bearing *Trilobatus sacculifer* (Foster et al., 2012). For deeper mixed-layer *G. kugleri*, we apply a calibration based on the similarly deeper-dwelling symbiont-bearing species *O. universa* (Henehan, Foster, et al., 2016). For *G. index*, which lacks any gradient in $\delta^{13}C$ with size (Fig. 3b), we apply the symbiont-barren calibration for *G. bulloides* (Martínez-Botí et al., 2015). In each case, calibration lines were adjusted to account for a middle Eocene seawater $\delta^{11}B$ ($\delta^{11}B_{sw}$) of 38.7 ‰ using the approach of Greenop et al. (2019). This is necessary, as otherwise modern calibrations conflate the effects of pH and $\delta^{11}B_{sw}$ on deep-time records (see Greenop et al., 2019 for more details).

We note also that reduced body size-$\delta^{13}C$ gradients in *Acarinina* during peak MECO at ODP Sites 1051 and 748 have been interpreted as symbiont 'bleaching' (Edgar et al., 2013; see also Wade et al., 2008). Since this could modify the pH of the foraminiferal microenvironment and artificially produce or accentuate a surface ocean pH drop, we tested whether bleaching occurred at the MECO by examining body size-$\delta^{13}C$ gradients at tropical ODP Sites 865 and 1260, where temperature-driven 'bleaching' might be most evident. However, we found no evidence for a reduction in either the $\delta^{13}C$ gradient between symbiont-bearing and symbiont-barren taxa or the body size-$\delta^{13}C$ gradient in the species analysed here (Fig. S2). This suggests that a loss of symbionts did not occur at these low-latitude sites, and that any $\delta^{11}B$ changes should therefore reflect changes in ambient seawater pH rather than changing vital effects.

2.5 pH and Temperature Calculations and Uncertainty Propagation

To calculate pH accurately from $\delta^{11}B$, a number of auxiliary parameters are required, including $\delta^{11}B_{sw}$, salinity and temperature. Using the approaches of Anagnostou et al. (2016) (namely assuming reasonable bounds on surface ocean saturation and vertical DIC gradients) and a $\delta^{11}B_{sw}$-corrected *T. sacculifer* calibration for their mixed layer-dwelling, symbiont-bearing early and middle Eocene foraminifera, we calculate absolute bounds of $\delta^{11}B_{sw}$ of 38.5 – 38.9 ‰ at this time. We assign a salinity of 34 ± 1 psu to all samples (note this parameter has only a small effect on pH and pCO_2 estimates (e.g. Henehan et al., 2013)). To estimate sea surface temperature, we used planktic foraminiferal Mg/Ca ratios, as they appear more robust in the face of diagenetic recrystallisation than $\delta^{18}O$ (Sexton, Wilson, & Pearson, 2006a). However, modern Mg/Ca-temperature calibrations cannot be directly applied to middle Eocene foraminifera, because of the different Mg/Ca_{sw} at this time and the (sizeable) effect of pH on foraminiferal Mg/Ca (e.g. Evans, Wade, et al., 2016; Gray & Evans, 2019). All our temperature calculations are therefore corrected for the non-linear response of foraminiferal Mg/Ca to changing Mg/Ca_{sw} following Evans, Brierley et al. (2016). Since pH calculations require temperature estimates, and vice versa, we iteratively correct both parameters, similar to methods given by Gray and Evans (2019). Low Eocene seawater pH means that pH corrections on Mg/Ca-derived temperatures are sizeable (Fig. S3). To our knowledge, these are the first Mg/Ca_{sw} and pH-corrected temperatures for this period, and thus provide new constraints on sea surface temperatures across a latitudinal gradient in the middle Eocene.

For uncertainty propagation, we used Monte Carlo simulations in R (R Core Team, 2015). For pH estimates, 500 $\delta^{11}B_{calcite}$ values were randomly generated from within a normal distribution described by 2σ analytical reproducibility for each data-point (see Table 1). Each value was then converted to $\delta^{11}B_{borate}$ according to each species' $\delta^{11}B_{sw}$-specific calibration (see Section 2.4). Major-ion chemistry-specific equilibrium constants (from Hain et al., 2015) for each value were calculated according to preliminary Mg/Ca-derived temperatures (from 500 simulations of Mg/Ca within 3% analytical uncertainty, corrected for Mg/Ca_{sw} (Evans, Brierley, et al., 2016), but not pH (Evans, Wade, et al., 2016), and 500 randomly-generated values of salinity (within 34 ± 1). pH was then calculated for each simulated value, and used to derive the 'excess Mg/Ca' due to low pH (according to the linear fit of Evans, Wade, et al. (2016)). pH-corrected temperatures were then calculated for each Monte

Carlo replicate, and subsequently used to re-calculate equilibrium constants and pH. This was iterated until simulated replicates converged on a unique solution to within 0.002 pH. Final temperature and pH estimates were calculated as the mean of the 500 Monte Carlo simulations, with 95% inter-quantile range of these replicates taken as uncertainty. In these calculations, we include uniformly distributed uncertainty on $\delta^{11}B_{sw}$ within the range of 38.5 – 38.9 ‰ (Anagnostou et al., 2016), when presenting true uncertainty on absolute values of pH. However, the long residence time of boron in the ocean (~10 to 20 Myr) means that $\delta^{11}B_{sw}$ would have remained constant across the time interval studied here, and so uncertainty on relative changes in pH is considerably smaller. To isolate the effect of $\delta^{11}B_{sw}$ on relative pH changes, and provide the basis for LOSCAR simulations discussed later in Section 2.7, we also calculated pH across a range of discrete values of $\delta^{11}B_{sw}$. We do not attempt to propagate uncertainty in Eocene major ion chemistry or (small) salinity effects on foraminiferal Mg/Ca (Hönisch et al., 2013) since quantitative constraints over this interval are limited.

2.6 pCO_2 calculations

To calculate pCO_2 from surface ocean pH, one requires one other carbonate system parameter (Zeebe & Wolf-Gladrow, 2001). Because we have no suitable proxy record to obtain this second parameter, we explore a number of possible scenarios using simplified assumptions to represent end-member pCO_2 possibilities. Firstly, we calculate pCO_2 assuming a constant calcite saturation state ($\Omega_{calcite}$) in the surface ocean at each site. This assumption represents a scenario in which alkalinity increases driven by elevated silicate weathering and carbonate dissolution could effectively keep pace with the pH decline calculated from $\delta^{11}B$. Specifically, in our Monte Carlo simulations we allow starting $\Omega_{calcite}$ to vary within a uniform distribution between 5.75 and 7.5 at Sites 865 and 1260, 5.25 and 7.25 at Site 1263, and 3.75 and 5.25 at Site 702, with differences reflecting each site's paleolatitude (following Anagnostou et al., 2016). For each Monte Carlo simulation, $\Omega_{calcite}$ was then held constant through the MECO, and the carbonate system solved to calculate pCO_2, according to the carbonate equilibrium constants and calcite solubility product calculated for each data point.

As a second end-member scenario, we performed pCO_2 calculations using the assumption that surface ocean total alkalinity (TAlk) remained constant throughout the event. By contrast with the

constant-$\Omega_{calcite}$ scenario, this assumption implies that silicate weathering and carbonate compensation were too weak to significantly affect surface ocean carbonate chemistry during the MECO, and that changes in pH reflect the addition of DIC alone. This assumption of constant TAlk would be more consistent with a postulated weakened silicate weathering feedback strength across the MECO (van der Ploeg et al., 2018). To obtain a pre-event surface ocean TAlk estimate, we took pre-event equilibrium values from simulations of the geochemical box model LOSCAR, matched to pre-event mean LOESS pH fit (see Section 2.7 below). We then held this alkalinity constant at within ±150 μmol of LOSCAR's pre-MECO surface ocean TAlk estimate throughout the MECO.

2.7 Carbon cycle modeling MECO acidification

Regrettably, the complex, spatially variable and as-yet poorly-constrained array of potential influences on carbonate $\delta^{13}C$ values during the MECO mean that reverse modelling the event (for example, as done for the PETM by Gutjahr et al., 2017) is not yet feasible. However, because LOSCAR (Long-term Ocean Sediment Carbon Reservoir, v2.0.4; Zeebe, 2012) approximates some critical processes for interpreting pH records - namely the changes in chemical weathering and carbonate burial one would normally associate with pCO_2 rise - we could use it to further explore feasible changes in pCO_2 over the MECO across a broad range of possible $\delta^{11}B_{sw}$. More specifically, we leveraged LOSCAR to obtain estimates for pCO_2 from MECO carbon cycle model scenarios that were constrained only by $\delta^{11}B$-derived pH. To do this we used LOSCAR's 'PALEO' configuration (with a Tethys ocean, and Paleogene circulation patterns and bathymetry), but with some modifications. Firstly, we replaced the default corrections for [Mg] and [Ca] (Ben-Yaakov & Goldhaber, 1973) with updated equilibrium constants that better quantify ion pairing effects (Hain et al., 2015) by accounting for the activities of all ions in solution using the larger and more up-to-date MIAMI database (Millero & Pierrot, 1998), using a seawater [Mg] and [Ca] of 38 and 17 mM, respectively. Secondly, to more finely resolve deep-water carbonate dissolution and compensation depth, we modelled one sediment level every 100 m, rather than the default 500 m (following Henehan, Hull, et al., 2016).

To obtain pre-MECO alkalinity estimates for any given $\delta^{11}B_{sw}$ scenario, the model was equilibrated by adjusting equilibrium pCO_2 in 10 Myr-long spin-up runs with a default-strength silicate weathering feedback (N_{Si} = 0.2) until we attained a fit between LOSCAR's low-latitude surface Pacific box and boron-derived pre-MECO surface ocean pH values (to within 0.002 pH units). This target pH for a given $\delta^{11}B_{sw}$ was calculated as the mean of the first 17 values of the mean LOESS fit prior to the pH drop at the peak MECO. For each value of $\delta^{11}B_{sw}$/starting pH, we then iteratively added different masses of CO_2 to the atmosphere over the timescale of our peak-MECO pH excursion (~ 100 kyr) until we produced a surface Pacific pH decrease that matched the minimum value in the $\delta^{11}B$-derived LOESS pH curve to within 0.002 pH units. This exercise was repeated across a broad range of $\delta^{11}B_{sw}$ (37.4 – 39.5 ‰), and in each case ΔpCO_2 was calculated as the difference in pCO_2 from spin-up to peak MECO. CO_2 forcing change (ΔF) was then calculated from ΔpCO_2, according to the relationship of Myhre et al. (1998). Our primary simulations used default parameterized climate sensitivity in LOSCAR of 3 ˚C warming per doubling of atmospheric pCO_2. Since calculated warming influences CO_2 solubility, DIC speciation and carbonate solubility calculations in LOSCAR, we also repeated our experiments with a prescribed 2˚C warming over the 100 kyr carbon-release event to test for the influence of this parameter, with negligible effect on our CO_2 estimates (at $\delta^{11}B_{sw}$ = 38.7 ‰, ΔpCO_2 changes by < 0.002 doublings).

3. Results

3.1 Boron isotope records

Boron isotope measurements are shown in Figure 4. The main feature of our record at our main site, ODP Site 865, is a transient ~1 ‰ $\delta^{11}B$ decrease focused around minimum MECO $\delta^{18}O$ values (~ 40.22 - 40.10 Ma, hereafter 'peak MECO'), followed by return to pre-event values (Fig. 4). Despite some discrepancies (Fig. 4b-d), our lower-resolution sites generally corroborate the observed trends at Site 865 well, especially when considering the stratigraphic challenges of correlating each record (see e.g. Fig. S1). With no further assumptions, this drop in $\delta^{11}B$ values constitutes the first empirical evidence for surface ocean acidification over the MECO, and at face value supports a rise of atmospheric pCO_2 associated with the event. Notably, though, the $\delta^{11}B$ excursion at peak MECO

where our samples are best resolved is brief (~120 kyr from onset to recovery), with limited, if any, change during the preceding ~280 kyr of global $\delta^{18}O$ decline (~ 40.5 - 40.22 Ma, hereafter 'MECO onset').

3.2 Calculated pH change at the MECO

To examine whether our choices of vital effect calibrations are reasonable, we compare pH calculated from $\delta^{11}B$ with and without consideration of vital effects in Fig. 5. We observe very large latitudinal offsets in $\delta^{11}B$ values (~3.3 ‰; Fig. 4). Without applying calibrations for vital effects at the MECO, even accounting for temperature (and hence pK^*_B) variations with latitude, gives a latitudinal pH gradient of up to 1.2 (Fig. 5a), that cannot reasonably be explained even considering a possibly deeper depth habitat for *G. index*. Such a large pH offset would translate to considerable $[CO_2]_{aq}$ variation between sites, and CO_2 disequilibrium between ocean and atmosphere of >4,500 µatm CO_2 at Site 702 (for Alkalinity > 1000 µmol/kg), which is not plausible. Besides this, at the pH values inferred at Site 702, for an ocean alkalinity ranging from 1,000 - 3,000 µmol/kg, $\Omega_{calcite}$ would reach as low as 0.2 - 0.4 at peak MECO. This would require *G. index* and other calcifiers at Site 702 to have persisted in waters highly undersaturated with respect to calcite, with few if any analogues for such behaviour today. In contrast, our pH estimates agree closely once vital effects are accounted for as described above (Fig. 5b), suggesting our assignment of calibrations from modern analogue species according to $\delta^{13}C$ and $\delta^{18}O$ is reasonable. These data therefore indicate that vital effects in foraminiferal $\delta^{11}B$ were present at least in middle Eocene globigerinathekids, and thus may well have been present in other extinct species too. We note, however, that the magnitude of vital effects in *A. praetopilensis* and *M. crassatus* predicted by the Foster et al. (2012) *T. sacculifer* calibration is very small, and so the agreement between calibrated globigerinathekids and uncalibrated *A. praetopilensis* and *M. crassatus* is not significantly worse than when modern analogue calibrations are applied to all species (see Fig. S4). Further research, considering among other things changes in $\delta^{11}B$ with size fraction (see e.g. Henehan, Foster, et al., 2016), is therefore required to determine whether modern analogue calibrations must be applied to *Morozovella* and *Acarinina* species.

As with any geological observation, corroboration of a signal at multiple sites globally allows more confidence in results. Additionally, multisite analyses allow us to test the feasibility of vital effect corrections in the Eocene (Figure 5), reducing an otherwise large structural uncertainty in our pH and pCO_2 estimates. However, combining data from four geographically disparate sites as we do here does present complications, with the obvious introduction of aliasing (Pisias & Mix, 1988) from our low-resolution sites (e.g. ODP Site 1260, where the peak MECO is not sampled), noise from uncertainty in stratigraphic correlation (e.g. see Fig. S1), and possible regional hydrographic differences (e.g. variable productivity, and hence perhaps air-sea disequilibrium, at ODP Site 1263 over the MECO (Boscolo Galazzo et al., 2015)). In all likelihood, all of these processes are at work within our records. The inter-site pH variability, taken at face value, at any given time within our record (Fig. 5) is sometimes larger than could easily be simulated with earth system models, suggesting inaccuracy in stratigraphic correlation likely plays a role in adding noise to our record. Consequently, so as not to risk over-interpreting scatter from these various sources of error at any one site, and to facilitate modelling work, we calculate a smoothed, globally-averaged surface ocean ΔpH LOESS curve for the MECO (Fig. 6).

To calculate the LOESS curve, we combined all sites' δ^{11}B-pH measurements using a best-fit LOESS where the degree of smoothing was optimized using a generalized cross validation algorithm (Golub et al., 1979) which objectively gauges the most statistically-supported value for the LOESS span (using code from M. Friendly, http://www.datavis.ca). Because the rates of pH change are important, we incorporated some uncertainty in the age domain, based on the sedimentation rate estimates between tie points, along with uncertainty in calculated pH. Specifically, 500 independent LOESS lines were fitted to each of the 500 replicate Monte Carlo pH datasets outlined above, with 500 simulated ages for each data-point generated from within the age range of the sampling interval. For a $\delta^{11}B_{sw}$ of 38.5-38.9 ‰, our data indicate a pH decrease of 0.12 ± 0.04 over <100 kyr coincident with the peak MECO (Fig. 6). The objective smoothing algorithm used in our global LOESS fit does however dampen the transient reduction of up to ~0.18 pH units implied by a single point at our most highly-resolved site, ODP 865 (Fig. 4), and so it is possible that further higher resolution studies may find our estimates of pH change to be conservative.

A somewhat surprising aspect of our LOESS global mean pH record is the lack of a pronounced decline in mean ocean pH during the onset phase of the MECO, when global temperature records suggest gradual warming (e.g. Bohaty et al., 2009). There are some apparent discrepancies between sample sites during this interval: at ODP Site 1263 $\delta^{11}B$ drops more in line with global $\delta^{18}O$ decline than observed at Sites 865 or 1260. However, since higher resolution sites show no such rise, and statistically none of the four sites show a significant trend in pH before the peak of the MECO (Fig. S5), we avoid overinterpreting inter-site differences here.

3.3 pCO_2 change over the MECO

pCO_2 calculated from surface ocean pH is shown for a constant saturation state (Fig 7a) and a constant LOSCAR-derived TAlk of 1750 ± 150 µmol/kg (Fig 7b). In the case of a constant Ω, pre-MECO pCO_2 (as defined in this instance as the mean of the LOESS values during the earliest 17 pre-MECO data points) is ~669 ± 145 µatm, with the maximum of the pCO_2 LOESS rising to ~1062 ± 127 µatm at the peak-MECO (equating to $0.67^{+0.17}_{-0.12}$ doublings). Assuming a constant (±150 µmol/kg) alkalinity instead, our boron isotope data would suggest a pCO_2 rise from ~563 ± 67 µatm to ~770 ± 62 µatm at the peak-MECO, a rise that is ~47% smaller than if calcite saturation remained constant. As these two end-member scenarios represent extreme limits to the possible real-world response, we suggest that the pCO_2 increase during the MECO was likely somewhere between these two scenarios.

From our LOSCAR simulations (Fig. 8) it may be seen that while absolute values of pCO_2 calculated are sensitive to $\delta^{11}B_{sw}$ (Fig. 8b), relative change in greenhouse forcing in terms of CO_2 doublings is relatively insensitive to changes in this parameter (i.e. 0.55 to 0.75 CO_2 doublings for $\delta^{11}B_{sw}$ between 37.5 and 39.5 ‰; Fig. 8c). This has been similarly demonstrated at the Eocene-Oligocene transition (Pearson et al., 2009) and at the PETM (Penman & Zachos, 2018). Using our LOSCAR modelling approach, instead of assuming constant $\Omega_{calcite}$ or alkalinity, our best-estimate middle Eocene $\delta^{11}B_{sw}$ range of 38.5 – 38.9 ‰ produces ΔpCO_2 scenarios from pre-MECO (i.e. background) to the peak MECO of 500 µatm rising to 765 µatm for a $\delta^{11}B_{sw}$ of 38.5‰, and 630 µatm rising to 990 µatm for a $\delta^{11}B_{sw}$ of 38.9 ‰ (Fig. 8b). Expressed as doublings of CO_2, these end-member scenarios for ΔpCO_2 equate to between 0.62 and 0.67, which translates to a CO_2 forcing change (ΔF)

of between 2.3 and 2.5 W m^{-2} (Fig. 8c). To quantify the absolute uncertainty bounds on pCO_2 within our best-estimate range of $\delta^{11}B_{sw}$ we repeated these LOSCAR modelling exercises for 1 and 2 se of the 500 Monte Carlo LOESS values for pre-event pH and peak-MECO pH minimum (i.e. grey shaded regions in Fig. 6), to calculate a pre-event pCO_2 of 565^{+110}_{-80}, and a peak MECO pCO_2 of 880^{+130}_{-100}, as plotted in Fig. S6. These pre-MECO pCO_2 levels are somewhat lower in an absolute sense compared to those values calculated assuming constant, pre-ascribed $\Omega_{calcite}$. This is because our LOSCAR simulations produce values of $\Omega_{calcite}$ in the surface Pacific of ~5 throughout the MECO, which is on the lowest end of our assumed feasible Eocene range of $\Omega_{calcite}$ and thus implies lower equilibrium TAlk values at this time. However, despite this difference in absolute values, a rise of $0.67^{+0.17}_{-0.12}$ doublings for the constant $\Omega_{calcite}$ scenario falls squarely in the range of estimates produced by LOSCAR. By contrast, assuming constant alkalinity produces a relatively smaller rise in pCO_2 upon a similar pre-MECO baseline ($0.45^{+0.06}_{-0.05}$), because without any concurrent rise in TAlk, a smaller rise in DIC is required to affect the same change in pH.

3. Discussion

4.1. MECO CO_2 change and carbon cycling

Our new boron isotope record helps to resolve some enigmatic features of the MECO. For example, an abrupt (< 10 kyr) rise in atmospheric pCO_2 centered around the peak of the MECO (Fig. 7) could help to explain why the CCD shoaled even at the peak of a ~400 kyr interval of apparent gradual warming - a key element of the so-called MECO 'carbon cycle conundrum' (Sluijs et al., 2013). A shorter CO_2 pulse could have surpassed the timescales on which chemical weathering responds to maintain oceanic $CaCO_3$ saturation state (~10^4-10^5 yr) (Colbourn et al., 2015), thereby prompting deep-sea carbonate dissolution similar to that seen during hyperthermals (e.g. Zachos et al., 2005). The source of such a carbon injection remains enigmatic however, particularly given the lack of any global excursion towards negative $\delta^{13}C$ at this time (Bohaty et al., 2009; Boscolo Galazzo et al., 2014; Edgar et al., 2010). Our lower estimates for background pCO_2 and change in pCO_2 over the MECO relative to previous reconstructions (Bijl et al., 2010) alleviate this problem somewhat, in necessitating lower masses of CO_2 injection into, and removal from, the surface ocean-atmosphere system. This also helps

to reconcile a rapid cooling and drawdown of CO_2 after the MECO with the absence of any carbonate overshoot due to silicate weathering, such as is seen at the PETM (Penman et al., 2016). We note that enhanced burial of organic carbon, such as is observed in the Peri-Tethys of Italy (Spofforth et al., 2010) and the Crimea-Caucasus (Benyamovskiy, 2012), and consistent with globally increased $\delta^{13}C$ in carbonates following the MECO (Bohaty et al., 2009), may have also played an important role in carbon drawdown.

Our finding that there was limited change in atmospheric pCO_2 during the onset phase of the MECO, however, even while carbonate $\delta^{18}O$ (Bohaty et al., 2009) and biomarker-based proxies (Bijl et al., 2010; Cramwinckel et al., 2018) suggest global temperatures were rising steadily over >200kyr, is a notable feature. To place a probabilistic bound on the maximum pCO_2 rise permitted by our data during the onset interval, we used a Monte Carlo approach, simulating 1000 datasets of pH across the 'MECO onset' (40.5 - 40.21 Ma) at our preferred estimate of $\delta^{11}B_{sw}$ by randomly sampling within the range of uncertainty of each data-point. We couple these to a constant approximate pre-MECO surface ocean alkalinity estimate from LOSCAR (1750 ±150 µmol/kg) to calculate the trend in pCO_2 predicted over the MECO onset interval. Using this approach, the mean simulated ΔpCO_2 over the MECO onset was +29 µatm. In the parlance of the IPCC (IPCC Core Writing Team, 2014), we find that an increase of > 230 µatm (~0.4 doublings) would be very unlikely (i.e. < 5% chance, see Fig. S7). Reconciling this small a magnitude of pCO_2 change with warming of ~3˚C, we suggest, would require one (or a combination of) a) very high climate sensitivity to CO_2 in the middle Eocene and/or some non-CO_2 climate forcing, b) dynamic changes in ocean alkalinity that we do not properly account for during the onset of the MECO, or c) a non-thermal (i.e. ice volume) component to carbonate $\delta^{18}O$ change.

While calculating a precise estimate of climate sensitivity is difficult given the limited spatial coverage of available surface temperature records, the observed ~0.5‰ decrease in benthic foraminiferal $\delta^{18}O$ values could equate to ~2 ˚C global mean surface temperature change using the relationships for the pre-Pleistocene described by Hanson et al. (2013), assuming no ice volume component. Using our upper limit of 0.3 CO_2 doublings during the MECO onset we would estimate an Earth System sensitivity of >6.7 ˚K per CO_2 doubling. Such sensitivity would be far higher than model

545 estimates of equilibrium climate sensitivity (IPCC Core Writing Team, 2014), and well outside of the
546 range of climate sensitivities previously calculated over the Cenozoic (Rohling & Members, 2012).
547 Moreover, any such heightened climate sensitivity would have to have lowered again at the peak
548 MECO, otherwise a 0.65 doubling of pCO_2 would have produced >4 ˚C of warming on top of the
549 gradual MECO warming trend; something which is not observed in marine temperature records.
550 Large-scale changes in ocean alkalinity are another hypothetical candidate for raising
551 atmospheric CO_2 without detectable change in surface pH (and thus foraminiferal $\delta^{11}B$) during the
552 MECO onset. A reduction in surface ocean TAlk might be possible over the MECO interval if there
553 were a reduction in silicate weathering, as suggested by Os isotopes and the observed shallowing of
554 the CCD (van der Ploeg et al., 2018). However, without a concurrent reduction in DIC, such a scenario
555 would be associated also with a reduction in global surface ocean pH, for which we see little evidence.
556 For surface ocean aqueous pCO_2, and hence atmospheric pCO_2, to have risen without significant pH
557 change, TAlk and dissolved inorganic carbon (DIC) would have had to *rise* in a ratio of approximately
558 1:0.9. A process (or processes) by which such stoichiometry would arise is unclear, and might
559 necessitate a complex combination of weathering fluxes and organic carbon burial fluxes. However,
560 all else being equal, such a rise in ocean TAlk and DIC would have increased deep ocean carbonate
561 saturation state, counter to observed MECO CCD change indicative of decreased saturation. Moreover,
562 alkalinity would have to increase by ~1000 µmol/kg, and [DIC] by ~900 µmol/kg to increase pCO_2 by
563 300 µatm: magnitudes which seem unfeasibly large to reconcile with a lack of pronounced shift in
564 $\delta^{13}C$. Thus while possible factors controlling alkalinity such as dynamic changes in calcification fluxes
565 (Boudreau et al., 2018; Henehan, Hull, et al., 2016) or sulfide oxidation (Calmels et al., 2014; Torres
566 et al., 2017) merit further investigation with more complex earth system models, at this stage it seems
567 difficult to decouple pH and pCO_2 during the MECO onset given the constraints of the marine
568 carbonate cycle.
569 Alternatively, it is possible that there was some contribution from ice melt to the trend towards
570 more negative $\delta^{18}O$ during the MECO onset, as has been hypothesized elsewhere (e.g. Tripati et al.,
571 2005; Lyle et al., 2005). Besides amplifying changes in carbonate $\delta^{18}O$, ice growth and subsequent
572 melt can also provide a mechanism to explain CCD change, by changing the balance of carbonate

burial onto shelves vs. the deep sea through sea level fluctuation (Lyle et al., 2005; Sluijs et al., 2013). As yet, however, evidence for earlier, pre-MECO glaciation is only suggestive, and not conclusive. Certainly, some high-latitude influence on climate and carbon cycle at this time is evidenced by a strengthened influence of obliquity in climate records (Bosboom et al., 2014; Westerhold et al., 2014). Furthermore, the second 'MECO-like' event shown in Fig. 1 does roughly coincide with a known ephemeral Antarctic glaciation event at ~37.3 Ma (Scher et al., 2014 and references within), perhaps by analogy lending some suggestive support for dynamic ice also around the MECO. A steeper slope in the relationship between high-latitude TEX_{86} and $\delta^{18}O$ in the middle Eocene compared to the early Eocene (Bijl et al., 2009), and comparison of Mg/Ca and $\delta^{18}O$ (Billups & Schrag, 2003; Dawber & Tripati, 2011; Lear, 2000) could also support an additive non-thermal component to seawater $\delta^{18}O$ fluctuations beginning prior to the MECO. Furthermore, although glaciation thresholds are highly model-specific (Gasson et al., 2014) most general circulation models (GCMs) simulate some continental ice on Antarctica (e.g. DeConto & Pollard, 2003; Gasson et al., 2014) at pre-MECO pCO_2 (e.g. Anagnostou et al., 2016). Temperature proxy records from the distal Antarctic peninsula (paleolatitude ~70˚; van Hinsbergen et al., 2015) indicate coastal mean annual temperatures of ~10-15 ˚C prior to the MECO (Douglas et al., 2014; Judd et al., 2019), which when scaled to the continental interior should have been sufficiently cold to prompt glacial inception in the Gamburtsev mountains (Rose et al., 2013). Additionally, various lines of sedimentological, micropaleontological and seismographic evidence (of varying degrees of certitude) exist for alpine or marine-terminating glaciers on Antarctica prior to or around the MECO (e.g. Birkenmajer, 1991; Ehrmann & Mackensen, 1992; Eittreim et al., 1995; Gulick et al., 2017; Margolis & Kennett, 1970), although we note that recently some of these interpretations have been contested (Sauermilch et al., 2019). Further, while we stress that extensive northern hemisphere ice sheets were not present (Edgar et al., 2007), indicators for middle Eocene Arctic sea ice (Darby, 2014; Eldrett et al., 2007; Stickley et al., 2009; Tripati et al., 2008) would seem incongruous with an ice-free Antarctic interior. Finally, the onset of synchronous changes in inferred sea level and $\delta^{18}O$ (Browning et al., 1996; Dawber et al., 2011; Pekar et al., 2005) that follow 1.2 Myr obliquity cycles (Boulila et al., 2011) coincides with an inflection in the relationship between estimated sea level and global deep-sea temperatures around 42-44 Ma (Gasson

et al., 2012; Kominz et al., 2008; Lear, 2000) that would also support ice volume change. We note though, this is strongly reliant on Kominz et al.'s New Jersey margin sea level reconstruction being representative of global eustasy (Gasson et al., 2012), and in such marginal marine settings it is difficult to confidently distinguish global eustatic change from steric effects or sediment supply, especially given the flatter shelves likely present at this time (Sømme et al. 2009). In sum, then, possible contributions from dynamic ice in driving middle Eocene $\delta^{18}O$, $\delta^{13}C$ and CCD oscillations remain an open question, but would help to explain some features of the event.

If middle Eocene ice reservoirs were present, and were sensitive to orbital configuration, changes in ocean circulation, or small rises in pCO_2, ice melt during the MECO onset would have lowered $\delta^{18}O_{sw}$ and raised sea-level, and partitioned more carbonate deposition onto flooded shelves and away from the deep-ocean (Lyle et al., 2005; Sluijs et al., 2013; Tripati et al., 2005). Such a scenario could therefore reconcile our observed stable surface ocean pH, shoaling CCD and a decline in carbonate $\delta^{18}O$ during the MECO onset. On one hand our new estimates of pre-MECO pCO_2 fall well below most modelled thresholds required for significant Antarctic glaciation (although model dependent; Gasson et al., 2014), and evidence for sizeable glacio-eustatic fluctuations around this time (e.g. Browning et al., 1996) suggests this is not wholly unreasonable. On the other hand, as previously discussed, conclusive evidence for substantial middle Eocene ice reservoirs is still lacking. Furthermore, if the $\delta^{18}O$ of pre- MECO ice was similar to Antarctic ice at the Eocene-Oligocene transition (~34 Ma), when ice growth increased global $\delta^{18}O$ by 0.6 ± 0.15 ‰, if 0.4 – 0.5 ‰ (roughly half) of the global MECO $\delta^{18}O$ decrease were attributable to ice, pre-MECO ice volumes available to melt would have had to be sizeable (equivalent to ~ 50m of sea level). Such a large change is most likely unrealistic, and indeed our new Mg/Ca-based sea-surface temperatures of > 20 ˚C (Fig. 8) from ODP Site 702 at a paleolatitude of 55-60 ˚C (van Hinsbergen et al., 2015), seem hard to reconcile with such large volumes of ice. At this point, then, neither extreme Earth system sensitivity or unstable, large middle Eocene ice reservoirs can be unequivocally ruled out.

A prediction of the ice-melt hypothesis for the MECO onset is that other temperature proxies would show limited warming even as $\delta^{18}O$ was declining. Although any one site may of course be subject to local hydrographic changes, globally, a sizeable secular $\delta^{18}O_{sw}$ decline should be evident.

For our part, we can compare $\delta^{18}O$ and Mg/Ca-derived temperatures measured in the same samples of planktic foraminifera (Fig. 9). At Sites 865 and 1263, which includes our highest resolution site, there is indeed a marked decline in $\delta^{18}O$ before any change in Mg/Ca. However, at Site 702, Mg/Ca and $\delta^{18}O$ are more or less in-step, while at Site 1260 Mg/Ca shows no response with declining $\delta^{18}O$ values but indicates a sharp cooling at the peak. Published organic biomarker temperature proxies (TEX_{86} and U^{k}_{37}) should allow another means to test this hypothesis. In support of an elevated Earth system sensitivity scenario, bulk carbonate $\delta^{18}O$ and organic temperature proxies at ODP Site 1172 move more or less in unison (Bijl et al., 2010) during the period in which we see little change in global ocean pH. Lower-resolution TEX_{86} data over the MECO at nearby ODP Site 1170 also shows MECO warmth, albeit relatively more muted (Cramwinckel, Woelders, et al., 2019). However, a possible incursion of the warm East-Australian current into this area around the MECO is indicated by fossil assemblages (Cramwinckel, Woelders, et al., 2019), which may complicate these signals. At equatorial ODP Site 959 a clear MECO warming event is expressed in TEX_{86} (Cramwinckel et al., 2018), but differing sample resolution makes it difficult to discern how clear the correlation between bulk carbonate $\delta^{18}O$ and TEX_{86} is at this site (Cramwinckel, van der Ploeg, et al., 2019). Additionally, a lack of age model tie-points between 40.02 and 42.84 Ma at this site makes it difficult to definitively discern whether the warming expressed in TEX_{86} was gradual and began during the global MECO onset, or was rapid and focused around the peak MECO, when our boron isotope data indicate CO_2 rise. Finally, at ODP Site 1263, there is no apparent correlation between TEX_{86} and concurrent carbonate $\delta^{18}O$ values (Boscolo Galazzo et al., 2014). As yet, then, evidence is not sufficiently conclusive to definitively accept or reject the hypothesis of ice melt contribution to $\delta^{18}O$ change during the onset of the MECO. However, the extremely high climate sensitivity to pCO_2 otherwise implied by our boron data suggests a component of ice melt is a hypothesis worthy of further interrogation.

4.2 Caveats, Conclusions and Prospects

By combining with LOSCAR simulations, we derive boron-based estimates of pCO_2 between 40.21 – 41.0 Ma of ~550 µatm ($2\sigma^{+110}_{-80}$ µatm; see Fig S6) that provide a precise estimate of the

boundary conditions on which the MECO was superimposed. Additionally, our estimate of peak-MECO pCO_2 of ~870 µatm ($2\sigma^{+130}_{-100}$ µatm; see Fig S6) tightly constrains CO_2 forcing change (ΔF) to between 2.3 and 2.5 W m^{-2} (Fig. 8c). These data confirm the finding of Bijl et al. (2010) that there was a rise in pCO_2 over the MECO, albeit to a lower degree and superimposed upon a lower baseline pCO_2 than indicated by the alkenone δ^{13}C-pCO_2 proxy. A number of outstanding puzzles surrounding the MECO clearly remain, however. The question of reduced silicate weathering at the MECO (van der Ploeg et al., 2018) remains open, for example, and requires further investigation. A reduced silicate weathering feedback would have implications for our LOSCAR-derived pCO_2 estimates, in that we use default-configuration weathering in LOSCAR to predict the evolution of TAlk expected over the course of a 100kyr CO_2 injection, allowing us to convert pH to pCO_2. As demonstrated in Fig. 7, the effect of a reduced silicate weathering feedback over the MECO would be to necessitate a smaller mass of CO_2 to be input to effect the same change in ocean pH and δ^{11}B. However, there are a number of reasons why we do not attempt to explore this in greater depth with LOSCAR here. Firstly, while a temporarily weakened and subsequently reactivated silicate weathering feedback is an elegant hypothesis, it is not the only solution that could explain changes in Os isotopes and changes in CCD. For example, rising sea-level could conceivably partition more carbonate deposition onto shelves and shoal the CCD (as already demonstrated in LOSCAR; Sluijs et al., 2013) while simultaneously changing the relative contributions of radiogenic vs. non-radiogenic rocks to global weathering fluxes. Effects on marine Si-cycling, an often-overlooked implication of mechanisms that invoke a dynamic silicate weathering feedback, could provide an independent means to interrogate the hypothesis of reduced silicate weathering at the MECO. During earlier Paleocene and Eocene warming events, the silicate weathering feedback on land drove enhanced burial and preservation of biogenic silica in the oceans as Si input fluxes were elevated (Penman, 2016; Penman et al., 2019). By analogy, a weakened silicate weathering feedback prior to the MECO might predict reduced burial of silica in the middle Eocene ocean. However, opal mass accumulation rates in the Pacific were amongst their highest Eocene levels in radiolarian zones RP14 and RP15, preceding the MECO (Moore et al., 2008). Moreover, the response to the MECO in the North Atlantic (Witkowski et al., 2014), the Southern Ocean (Witkowski et al., 2012), and the equatorial Indian Ocean (Savian et al., 2016) was a

pronounced rise in the deposition/preservation of siliceous plankton, supportive perhaps of a global rise in marine [Si] concurrent with warming. These records do not therefore immediately appear consistent with a weakened silicate weathering feedback at the MECO. However, we would encourage further investigation into the magnitude and geographical extent of this enhanced silica burial, and to look for chert deposits analogous to those seen after earlier warming events (Penman, 2016; Penman et al., 2019) to independently test the weakened silicate-weathering hypothesis. Furthermore, interrogating other weathering-sensitive isotope systems such as Li, Si or Sr may help in further constraining changes in silicate weathering over this event.

Besides questions over the dynamics of the silicate weathering feedback, we suggest that even implementing a weakened and then restored silicate weathering feedback in LOSCAR (as in van der Ploeg et al., 2018) would not fully capture the complexity of the MECO event. In such simulations (e.g. Sluijs et al., 2013; van der Ploeg et al., 2018) CO_2 drawdown is not as rapid as the recovery of pH and global temperatures observed after the MECO, and is usually accompanied by an overshoot in simulated CCD, for which (at least in the Pacific and Indian Oceans) there is scant sedimentary evidence. This may suggest a role for organic matter burial (Moebius et al., 2015; Spofforth et al., 2010) and/or ocean carbon storage (Sexton et al., 2011). To simulate these forcings realistically, and to accurately reproduce MECO surface ocean $\delta^{13}C$ changes (which vary widely both in magnitude and direction of change globally), would require a more complex model with dynamic ocean circulation. In short it is likely that during the MECO and its recovery more complex biogeochemical feedbacks were at work than are represented in the LOSCAR simulations of Sluijs et al. (2013), Van der Ploeg (2018), or our current contribution. Therefore, we present our scenarios for MECO pCO_2 change as current best estimates, mindful that lower TAlk change due to weakened silicate weathering might reduce the required mass of C injection, but that higher sampling resolution around the short pH minimum (statistically underweighted in our global LOESS as it is defined by a single datapoint) might increase it.

In summary, these data offer robust independent confirmation of pCO_2 rise during the MECO, the bulk of which occurs at the peak of the 400 kyr event. Although our new pCO_2 estimates do not allow us to ascertain the causal driver of the MECO, a number of informative observations can be

made. Firstly, the mass of C that was transferred to and from the surface ocean-atmosphere system over the MECO was considerably smaller than that required to explain previous MECO ΔpCO_2 estimates based on the alkenone $\delta^{13}C$ proxy (Bijl et al., 2010), and if the silicate weathering feedback were diminished, this mass could be smaller still. This smaller mass could bring internal reorganization of carbon reservoirs into play in explaining the MECO, rather than invoking a large exogenous carbon injection. Secondly, the limited evidence we see globally for any substantial rise in pCO_2 during the onset stage of the MECO suggests a climate, and perhaps nascent cryosphere, that was highly sensitive to perturbation. While we suggest that a contribution to global $\delta^{18}O$ change from ice melt during the initial phase of the MECO may be the most parsimonious means to reconcile CCD shoaling and limited pCO_2 rise, we recognize that further work is required to ascertain the feasibility of such a scenario. For instance, more precise dating of glacial deposits and more extensive circum-Antarctic temperature proxy records are of vital importance. Furthermore, we encourage further comparison of $\delta^{18}O$ with concurrent independent temperature proxies (e.g. TEX_{86}, clumped isotopes) to further isolate $\delta^{18}O_{sw}$ change over the MECO. Modelling work to explore the potential $\delta^{18}O$ range of nascent middle Eocene ice would also be beneficial, to constrain the volumes of ice melt required. Finally, while a trigger for ice melt without significant pCO_2 rise is uncertain, we suggest that ocean circulation is a prime target for investigation, given a) spatially-variable bulk carbonate $\delta^{13}C$ changes (Bohaty et al., 2009), b) spatial variability in circum-Antarctic temperature (Douglas et al., 2014; Judd et al., 2019), c) geochemical and micropaleontological evidence for changing high-latitude ocean circulation (Cramwinckel, Woelders, et al., 2019; Scher & Delaney, 2010), and d) enhanced sensitivity of global thermohaline circulation to orbital configuration (Vahlenkamp et al., 2018) around the MECO. In sum, while our new estimates of pCO_2 across the MECO move our understanding of this event forward, there remains considerable work to be done to fully elucidate the drivers of this enigmatic event.

Acknowledgements

This research used samples provided by the International Ocean Discovery Program (IODP). We thank Steve Bohaty for assistance with stratigraphy, provision of sample material from Sites 702 and

741 1263, and helpful discussion. We thank Paul Wilson for providing access to washed sample residues
742 for Sites 1260. We thank Paige Breen for providing $\delta^{13}C$ and $\delta^{18}O$ data from IODP Site 1408. We
743 thank Tom Chalk for assistance with trace element analysis, and the rest of the B-Team at the
744 University of Southampton for their help and cooperation. We thank Bärbel Hönisch, Christopher
745 Pearce, David Evans and Mathis Hain for helpful discussion, and Ellen Thomas for providing
746 feedback on an earlier draft of the manuscript. We also thank Peter Bijl and one anonymous reviewer
747 for helpful feedback which improved the manuscript. Financial support was provided from via the
748 Yale Peabody Museum to MJH, a NERC Postdoctoral Research Fellowship (NE/H016457/1), NERC
749 Standard Grant (NE/P013112/1) and Leverhulme Early Career Fellowship (ECF-2013-608) to KME, a
750 Flint Postdoctoral Fellowship to DEP, and NERC grants awarded to PNP (NE/I005870/1) and GLF
751 (NE/I005595/1). We report no conflicts of interests for any co-authors. All data supporting our
752 conclusions is available in the supplementary materials, and is also archived on PANGAEA at
753 https://doi.pangaea.de/10.1594/PANGAEA.909432.
754

755 **Author contributions**

756 M.J.H. conducted boron isotope and trace element analyses, ran calculations and statistical tests, and
757 co-designed LOSCAR simulations. K.M.E. picked foram samples, developed the age models and ran
758 stable carbon and oxygen isotope analyses. M.J.H. and K.E. drafted figures and text. G.L.F. co-
759 directed the study and assisted in experimental design and data analysis. D.E.P. co-designed and ran
760 all LOSCAR simulations. P.M.H. co-directed modelling and writing, coordinated stable isotope data
761 collection from Site 1408 and edited the manuscript. R.G. and E.A. assisted in approximating vital
762 effects. E.A. helped in estimating external reproducibility and calculating our $\delta^{11}B_{sw}$ estimate. P.N.P.
763 co-directed the study and assisted with foraminiferal taxonomy. All authors discussed the results and
764 contributed to the final text.

765 **Figure Captions**
766

767 ***Figure 1.*** *Repeating patterns in $\delta^{13}C$ and $\delta^{18}O$ during the middle-late Eocene and early Oligocene are*
768 *evident in the benthic foraminiferal compilation of Cramer et al. (2009), here shown adjusted to the*

Geological Timescale 2012 (GTS2012; Gradstein et al., 2012). In each case, excursions towards higher benthic foraminiferal $\delta^{13}C$ coincide with instances where $\delta^{18}O$ changes diverge from the underlying trend of cooling and ice-growth in the middle-late Eocene. 'E-OT' as marked in the gray band denotes the Eocene-Oligocene transition.

***Figure 2:** Locations of our study sites (colored markers) on a continental reconstruction from ~40 Ma from www.odsn.de (Hay et al., 1999). The location of ODP Site 1172 (where alkenone-based pCO_2 reconstructions from Bijl et al. (2010) were derived) is also marked as a white star.*

***Figure 3.** Planktic foraminiferal stable oxygen (**a**) and carbon (**b**) isotope gradients with test size for species used in this study, measured at IODP Site 1408. Preliminary age assigned to this time-slice is between 40.0 and 40.5 Ma or planktic foraminiferal Zone E12. Thermocline dwelling, symbiont-barren species* Subbotina linaperta *and benthic foraminifera* Nuttallides truempyi *are shown for comparison.*

***Figure 4.** Measured planktic foraminiferal $\delta^{11}B$ at each site in the context of local $\delta^{13}C$ and $\delta^{18}O$ data. These data are as follows: (a) Benthic foraminiferal $\delta^{13}C$ and $\delta^{18}O$ data from ODP Site 865 (Edgar et al., (in prep.)); (b) Benthic foraminiferal $\delta^{13}C$ and $\delta^{18}O$ data from ODP Site 1260 (Edgar et al., 2010; Sexton, Wilson, & Norris, 2006); (c) Bulk sediment $\delta^{13}C$ and $\delta^{18}O$ data from ODP Site 1263 (Bohaty et al., 2009) and (d) Bulk sediment $\delta^{13}C$ and $\delta^{18}O$ data from ODP Site 702 (Bohaty et al., 2009). $\delta^{18}O$ data are shown in blue, $\delta^{13}C$ data is in grey, and $\delta^{11}B$ data are colored according to their site marker in Figure 1. Error bars on $\delta^{11}B$ data represent 2σ uncertainty estimated from ^{11}B signal intensity based on long term replicates of JCp-1 Porites coral standard (Okai et al., 2002) (see Methods).*

***Figure 5.** Boron-derived pH reconstructions from the four study sites without vital effect calibrations (**a**) and applying species-specific calibrations (**b**). Note these calculations assume $\delta^{11}B_{sw}$ of 38.5 - 38.9 ‰, $[Mg]_{sw}$= 38 mM, and $[Ca]_{sw}$= 17 mM, and temperature estimates from planktic foraminiferal Mg/Ca (see Section 2.5).*

***Figure 6.** Mean global surface ocean pH and pCO_2 change from boron isotopes. All sites are stacked to create a global loess-smoothed pH curve, shown in context of $\delta^{13}C$ and $\delta^{18}O$ values from bulk carbonate at ODP Site 702 (Bohaty et al., 2009) (the site to which other sites' age models are tied). Dark and light grey shaded areas represent 95 and 68% confidence intervals, respectively, as determined by 500 Monte Carlo simulations of LOESS fits on simulated datasets within the propagated uncertainty of each pH data-point. Calculations here are for a $\delta^{11}B_{sw}$ of 38.5-38.9 ‰.*

Figure 7. *pCO_2 across the MECO calculated assuming either constant surface ocean saturation state (panel a) or constant surface ocean alkalinity (panel b), for our best estimate of $\delta^{11}B_{sw}$ (38.5 – 38.9 ‰).*

Figure 8. *For each given value of $\delta^{11}B_{sw}$, calculated 'pre-event' pH values (solid blue line, the average of the pH values prior to the peak MECO excursion), and the minimum value reached by the global LOESS during peak MECO (dashed blue line) are shown in panel a. In panel b, the atmospheric pCO_2 required for LOSCAR to attain 'pre-event' pH values (solid red line and triangles) is shown. We then iteratively simulated injection of different carbon masses over the timescales of our pH drop (~ 100 kyr) until we attained a surface Pacific pH that matched the pH minimum in our LOESS curve calculated for that $\delta^{11}B_{sw}$, and noted the atmospheric pCO_2 attained by LOSCAR (dashed red line and inverted triangles). Panel c shows the change in pCO_2 in panel b, expressed in terms of CO_2 doublings, and as CO_2 forcing change, ΔF (calculated according to ref. (Myhre et al., 1998)). Our best estimate of $\delta^{11}B_{sw}$ (38.5 – 38.9 ‰) is shown by the vertical blue bar through a, b and c, and implies 0.6 - 0.7 doublings of pCO_2 over the MECO event.*

Figure 9. *Mg/Ca-derived temperatures and oxygen isotope ratios across the MECO (a-d). Note that these data are derived from subsamples of the same crushed foraminifera measured for $\delta^{11}B$. While two sites (panels a,b) do show a decoupling of $\delta^{18}O$ and Mg/Ca temperatures consistent with ice melt, two other sites do not (panels c, d). Site 1260 is particularly difficult to explain, and may well reflect the influence locally of secondary controls on one or both of the proxies.*

References

Abels, H. A., Clyde, W. C., Gingerich, P. D., Hilgen, F. J., Fricke, H. C., Bowen, G. J., & Lourens, L. J. (2012). Terrestrial carbon isotope excursions and biotic change during Palaeogene hyperthermals. *Nature Geoscience*, *5*(5), 326–329. https://doi.org/10.1038/ngeo1427

Anagnostou, E., John, E. H., Edgar, K. M., Foster, G. L., Ridgwell, A., Inglis, G. N., et al. (2016). Changing atmospheric CO2 concentration was the primary driver of early Cenozoic climate. *Nature*, *533*, 380–384. https://doi.org/10.1038/nature17423

Arreguín-Rodríguez, G. J., Alegret, L., & Thomas, E. (2016). Late Paleocene-middle Eocene benthic foraminifera on a Pacific seamount (Allison Guyot, ODP Site 865): Greenhouse climate and superimposed hyperthermal events: Benthic Foraminifera on Pacific Seamount. *Paleoceanography*, *31*(3), 346–364. https://doi.org/10.1002/2015PA002837

Barnet, J. S. K., Littler, K., Kroon, D., Leng, M. J., Westerhold, T., Röhl, U., & Zachos, J. C. (2018). A new high-resolution chronology for the late Maastrichtian warming event: Establishing

robust temporal links with the onset of Deccan volcanism. *Geology*, *46*(2), 147–150. https://doi.org/10.1130/G39771.1

Barnet, J. S. K., Littler, K., Westerhold, T., Kroon, D., Leng, M. J., Bailey, I., et al. (2019). A High-Fidelity Benthic Stable Isotope Record of Late Cretaceous–Early Eocene Climate Change and Carbon-Cycling. *Paleoceanography and Paleoclimatology*. https://doi.org/10.1029/2019PA003556

Ben-Yaakov, S., & Goldhaber, M. B. (1973). The influence of sea water composition on the apparent constants of the carbonate system. *Deep Sea Research and Oceanographic Abstracts*, *20*(1), 87–99. https://doi.org/10.1016/0011-7471(73)90044-2

Benyamovskiy, V. N. (2012). A high resolution Lutetian-Bartonian planktonic foraminiferal zonation in the Crimean-Caucasus region of the northeastern Peri-Tethys. *Austrian Journal of Earth Sciences*, *105*(1), 117–128.

Berner, R. A., Lasaga, A. C., & Garrels, R. M. (1983). The carbonate-silicate geochemical cycle and its effect on atmospheric carbon dioxide over the past 100 million years. *American Journal of Science*, *283*(7), 641–683. https://doi.org/10.2475/ajs.283.7.641

Bijl, P. K., Schouten, S., Sluijs, A., Reichart, G.-J., Zachos, J. C., & Brinkhuis, H. (2009). Early Palaeogene temperature evolution of the southwest Pacific Ocean. *Nature*, *461*(7265), 776–779. https://doi.org/10.1038/nature08399

Bijl, P. K., Houben, A. J. P., Schouten, S., Bohaty, S. M., Sluijs, A., Reichart, G.-J., et al. (2010). Transient Middle Eocene Atmospheric CO2 and Temperature Variations. *Science*, *330*(6005), 819–821. https://doi.org/10.1126/science.1193654

Billups, K., & Schrag, D. P. (2003). Application of benthic foraminiferal Mg/Ca ratios to questions of Cenozoic climate change. *Earth and Planetary Science Letters*, *209*(1–2), 181–195. https://doi.org/10.1016/S0012-821X(03)00067-0

Birch, H. S., Coxall, H. K., & Pearson, P. N. (2012). Evolutionary ecology of Early Paleocene planktonic foraminifera: size, depth habitat and symbiosis. *Paleobiology*, *38*(3), 374–390. https://doi.org/10.1666/11027.1

Birkenmajer, K. (1991). Tertiary glaciation in the South Shetland Islands, West Antarctica: evaluation of data. In M. R. A. Thomson, J. A. Crame, & J. W. Thomson (Eds.), *Geological Evolution of Antarctica* (pp. 629–632). Cambridge, UK: Cambridge University Press.

Bohaty, S. M., & Zachos, J. C. (2003). Significant Southern Ocean warming event in the late middle Eocene. *Geology*, *31*(11), 1017–1020. https://doi.org/10.1130/G19800.1

Bohaty, S. M., Zachos, J. C., Florindo, F., & Delaney, M. L. (2009). Coupled greenhouse warming and deep-sea acidification in the middle Eocene. *Paleoceanography*, *24*(2), PA2207. https://doi.org/10.1029/2008PA001676

Bosboom, R. E., Abels, H. A., Hoorn, C., van den Berg, B. C. J., Guo, Z., & Dupont-Nivet, G. (2014). Aridification in continental Asia after the Middle Eocene Climatic Optimum (MECO). *Earth and Planetary Science Letters*, *389*, 34–42. https://doi.org/10.1016/j.epsl.2013.12.014

Boscolo Galazzo, F., Thomas, E., Pagani, M., Warren, C., & Giusberti, L. (2014). The middle Eocene climatic optimum (MECO): A multiproxy record of paleoceanographic changes in the southeast Atlantic (ODP Site 1263, Walvis Ridge): MECO repercussions in the SE Atlantic. *Paleoceanography*, *29*(12), 1143–1161. https://doi.org/10.1002/2014PA002670

Boscolo Galazzo, F., Thomas, E., & Giusberti, L. (2015). Benthic foraminiferal response to the Middle Eocene Climatic Optimum (MECO) in the South-Eastern Atlantic (ODP Site 1263). *Palaeogeography, Palaeoclimatology, Palaeoecology*, *417*, 432–444. https://doi.org/10.1016/j.palaeo.2014.10.004

Boudreau, B. P., Middelburg, J. J., & Luo, Y. (2018). The role of calcification in carbonate compensation. *Nature Geoscience*, *11*(12), 894–900. https://doi.org/10.1038/s41561-018-0259-5

Boulila, S., Galbrun, B., Miller, K. G., Pekar, S. F., Browning, J. V., Laskar, J., & Wright, J. D. (2011). On the origin of Cenozoic and Mesozoic "third-order" eustatic sequences. *Earth-Science Reviews*, *109*(3–4), 94–112. https://doi.org/10.1016/j.earscirev.2011.09.003

Bralower, T. J., Zachos, J. C., Thomas, E., Parrow, M., Paull, C. K., Kelly, D. C., et al. (1995). Late Paleocene to Eocene paleoceanography of the equatorial Pacific Ocean: Stable isotopes recorded at Ocean Drilling Program Site 865, Allison Guyot. *Paleoceanography*, *10*(4), 841–865. https://doi.org/10.1029/95PA01143

Browning, J. V., Miller, K. G., & Pak, D. K. (1996). Global implications of lower to middle Eocene sequence boundaries on the New Jersey coastal plain: The icehouse cometh. *Geology*, *24*(7), 639. https://doi.org/10.1130/0091-7613(1996)024<0639:GIOLTM>2.3.CO;2

Calmels, D., Gaillardet, J., & François, L. (2014). Sensitivity of carbonate weathering to soil CO 2 production by biological activity along a temperate climate transect. *Chemical Geology*, *390*, 74–86. https://doi.org/10.1016/j.chemgeo.2014.10.010

Cameron, A. C., Gelbach, J. B., & Miller, D. L. (2008). Bootstrap-Based Improvements for Inference with Clustered Errors. *Review of Economics and Statistics*, *90*(3), 414–427. https://doi.org/10.1162/rest.90.3.414

Clement, B. M., & Hailwood, E. A. (1991). Magnetostratigraphy of Sediments from Sites 701 and 702. In P. F. Cieselski, Y. Kristoffersen, & et al. (Eds.), *Proceedings of the Ocean Drilling Program: Scientific Results* (Vol. 114, pp. 359–366).

Colbourn, G., Ridgwell, A., & Lenton, T. M. (2015). The time scale of the silicate weathering negative feedback on atmospheric CO_2. *Global Biogeochemical Cycles*, *29*(5), 583–596. https://doi.org/10.1002/2014GB005054

Cramer, B. S., Toggweiler, J. R., Wright, J. D., Katz, M. E., & Miller, K. G. (2009). Ocean overturning since the Late Cretaceous: Inferences from a new benthic foraminiferal isotope compilation. *Paleoceanography*, *24*(4), PA4216. https://doi.org/10.1029/2008PA001683

Cramwinckel, M. J., Huber, M., Kocken, I. J., Agnini, C., Bijl, P. K., Bohaty, S. M., et al. (2018). Synchronous tropical and polar temperature evolution in the Eocene. *Nature*, *559*(7714), 382–386. https://doi.org/10.1038/s41586-018-0272-2

Cramwinckel, M. J., van der Ploeg, R., Bijl, P. K., Peterse, F., Bohaty, S. M., Röhl, U., et al. (2019). Harmful algae and export production collapse in the equatorial Atlantic during the zenith of Middle Eocene Climatic Optimum warmth. *Geology*, *47*(3), 247–250. https://doi.org/10.1130/G45614.1

Cramwinckel, M. J., Woelders, L., Huurdeman, E. P., Peterse, F., Gallagher, S. J., Pross, J., et al. (2019). Surface-circulation change in the Southern Ocean across the Middle Eocene Climatic Optimum: inferences from dinoflagellate cysts and biomarker paleothermometry. *Climate of the Past Discussions*, 1–34. https://doi.org/10.5194/cp-2019-35

Darby, D. A. (2014). Ephemeral formation of perennial sea ice in the Arctic Ocean during the middle Eocene. *Nature Geoscience*, *7*(3), 210–213. https://doi.org/10.1038/ngeo2068

Dawber, C. F., & Tripati, A. K. (2011). Constraints on glaciation in the middle Eocene (46-37 Ma) from Ocean Drilling Program (ODP) Site 1209 in the tropical Pacific Ocean: GLACIATION IN THE MIDDLE EOCENE. *Paleoceanography*, *26*(2), n/a-n/a. https://doi.org/10.1029/2010PA002037

Dawber, C. F., Tripati, A. K., Gale, A. S., MacNiocaill, C., & Hesselbo, S. P. (2011). Glacioeustasy during the middle Eocene? Insights from the stratigraphy of the Hampshire Basin, UK. *Palaeogeography, Palaeoclimatology, Palaeoecology*, *300*(1–4), 84–100. https://doi.org/10.1016/j.palaeo.2010.12.012

DeConto, R. M., & Pollard, D. (2003). Rapid Cenozoic glaciation of Antarctica induced by declining atmospheric CO2. *Nature*, *421*(6920), 245–249. https://doi.org/10.1038/nature01290

D'Hondt, S., Zachos, J. C., & Schultz, G. (1994). Stable isotopic signals and photosymbiosis in Late Paleocene planktic foraminifera. *Paleobiology*, *20*(03), 391–406. https://doi.org/10.1017/S0094837300012847

Dickens, G. R., O'Neil, J. R., Rea, D. K., & Owen, R. M. (1995). Dissociation of oceanic methane hydrate as a cause of the carbon isotope excursion at the end of the Paleocene. *Paleoceanography*, *10*(6), 965–971. https://doi.org/10.1029/95PA02087

Douglas, P. M. J., Affek, H. P., Ivany, L. C., Houben, A. J. P., Sijp, W. P., Sluijs, A., et al. (2014). Pronounced zonal heterogeneity in Eocene southern high-latitude sea surface temperatures. *Proceedings of the National Academy of Sciences*, *111*(18), 6582–6587. https://doi.org/10.1073/pnas.1321441111

Edgar, K. M., Bohaty, S. M., Coxall, H. K., Bown, P. R., Batenburg, S. J., Lear, C. H. & Pearson, P. N. ((in prep.)). New composite section with bio- and isotope stratigraphies spanning the Middle Eocene Climatic Optimum from tropical ODP Site 865 in the Pacific Ocean.

Edgar, K. M., Wilson, P. A., Sexton, P. F., & Suganuma, Y. (2007). No extreme bipolar glaciation during the main Eocene calcite compensation shift. *Nature*, *448*(7156), 908–911. https://doi.org/10.1038/nature06053

Edgar, K. M., Wilson, P. A., Sexton, P. F., Gibbs, S. J., Roberts, A. P., & Norris, R. D. (2010). New biostratigraphic, magnetostratigraphic and isotopic insights into the Middle Eocene Climatic Optimum in low latitudes. *Palaeogeography, Palaeoclimatology, Palaeoecology*, *297*(3–4), 670–682. https://doi.org/10.1016/j.palaeo.2010.09.016

Edgar, K. M., Bohaty, S. M., Gibbs, G., Samantha J., Sexton, P. F., Norris, R. D., & Wilson, P. A. (2013). Symbiont 'bleaching' in planktic foraminifera during the Middle Eocene Climatic Optimum. *Geology*, *41*(1), 15–18. https://doi.org/10.1130/G33388.1

Edgar, K. M., Anagnostou, E., Pearson, P. N., & Foster, G. L. (2015). Assessing the impact of diagenesis on δ11B, δ13C, δ18O, Sr/Ca and B/Ca values in fossil planktic foraminiferal calcite. *Geochimica et Cosmochimica Acta*, *166*, 189–209. https://doi.org/10.1016/j.gca.2015.06.018

Ehrmann, W. U., & Mackensen, A. (1992). Sedimentological evidence for the formation of an East Antarctic ice sheet in Eocene/Oligocene time. *Palaeogeography, Palaeoclimatology, Palaeoecology*, *93*(1–2), 85–112. https://doi.org/10.1016/0031-0182(92)90185-8

Eittreim, S. L., Cooper, A. K., & Wannesson, J. (1995). Seismic stratigraphic evidence of ice-sheet advances on the Wilkes Land margin of Antarctica. *Sedimentary Geology*, *96*(1–2), 131–156. https://doi.org/10.1016/0037-0738(94)00130-M

Eldrett, J. S., Harding, I. C., Wilson, P. A., Butler, E., & Roberts, A. P. (2007). Continental ice in Greenland during the Eocene and Oligocene. *Nature*, *446*(7132), 176–179. https://doi.org/10.1038/nature05591

Evans, D., Brierley, C., Raymo, M. E., Erez, J., & Müller, W. (2016). Planktic foraminifera shell chemistry response to seawater chemistry: Pliocene–Pleistocene seawater Mg/Ca, temperature and sea level change. *Earth and Planetary Science Letters*, *438*, 139–148. https://doi.org/10.1016/j.epsl.2016.01.013

Evans, D., Wade, B. S., Henehan, M. J., Erez, J., & Müller, W. (2016). Revisiting carbonate chemistry controls on planktic foraminifera Mg/Ca: implications for sea surface temperature and hydrology shifts over the Paleocene–Eocene Thermal Maximum and Eocene–Oligocene transition. *Clim. Past*, *12*(4), 819–835. https://doi.org/10.5194/cp-12-819-2016

Ezard, T. H. G., Edgar, K. M., & Hull, P. M. (2015). Environmental and biological controls on size-specific $\delta^{13}C$ and $\delta^{18}O$ in recent planktonic foraminifera. *Paleoceanography*, *30*(3), 151–173. https://doi.org/10.1002/2014PA002735

Foster, G. L. (2008). Seawater pH, pCO_2 and [CO_3^{2-}] variations in the Caribbean Sea over the last 130kyr: A boron isotope and B/Ca study of planktic foraminifera. *Earth and Planetary Science Letters*, *271*(1–4), 254–266. https://doi.org/10.1016/j.epsl.2008.04.015

Foster, G. L., & Rae, J. W. B. (2016). Reconstructing Ocean pH with Boron Isotopes in Foraminifera. *Annual Review of Earth and Planetary Sciences*, *44*(1), 207–237. https://doi.org/10.1146/annurev-earth-060115-012226

Foster, G. L., Lear, C. H., & Rae, J. W. B. (2012). The evolution of pCO_2, ice volume and climate during the middle Miocene. *Earth and Planetary Science Letters*, *341–344*(0), 243–254. https://doi.org/10.1016/j.epsl.2012.06.007

Gasson, E., Siddall, M., Lunt, D. J., Rackham, O. J. L., Lear, C. H., & Pollard, D. (2012). Exploring uncertainties in the relationship between temperature, ice volume, and sea level over the past 50 million years. *Reviews of Geophysics*, *50*(1). https://doi.org/10.1029/2011RG000358

Gasson, E., Lunt, D. J., DeConto, R. M., Goldner, A., Heinemann, M., Huber, M., et al. (2014). Uncertainties in the modelled CO2 threshold for Antarctic glaciation. *Climate of the Past*, *10*(2), 451–466. https://doi.org/10.5194/cp-10-451-2014

Golub, G. H., Heath, M., & Wahba, G. (1979). Generalized Cross-Validation as a Method for Choosing a Good Ridge Parameter. *Technometrics*, *21*(2), 215–223. https://doi.org/10.1080/00401706.1979.10489751

Gradstein, F. M., Ogg, J. G., Schmitz, M., & Ogg, G. (2012). *The Geologic Time Scale 2012 2-Volume Set*. Elsevier.

Gray, W. R., & Evans, D. (2019). Nonthermal Influences on Mg/Ca in Planktonic Foraminifera: A Review of Culture Studies and Application to the Last Glacial Maximum. *Paleoceanography and Paleoclimatology*. https://doi.org/10.1029/2018PA003517

Greenop, R., Hain, M. P., Sosdian, S., Oliver, K. I. C., Goodwin, P., Chalk, T. B., et al. (2017). A record of Neogene seawater δ11B reconstructed from paired δ11B analyses on benthic and planktic foraminifera. *Climate of the Past*, *13*, 149–170. https://doi.org/doi:10.5194/cp-13-149-2017

Greenop, R., Sosdian, S. M., Henehan, M. J., Wilson, P. A., Lear, C. H., & Foster, G. L. (2019). Orbital Forcing, Ice Volume, and CO $_2$ Across the Oligocene-Miocene Transition. *Paleoceanography and Paleoclimatology*, *34*(3), 316–328. https://doi.org/10.1029/2018PA003420

Gulick, S. P. S., Shevenell, A. E., Montelli, A., Fernandez, R., Smith, C., Warny, S., et al. (2017). Initiation and long-term instability of the East Antarctic Ice Sheet. *Nature*, *552*(7684), 225–229. https://doi.org/10.1038/nature25026

Gutjahr, M., Ridgwell, A., Sexton, P. F., Anagnostou, E., Pearson, P. N., Pälike, H., et al. (2017). Very large release of mostly volcanic carbon during the Palaeocene–Eocene Thermal Maximum. *Nature*, *548*(7669), nature23646. https://doi.org/10.1038/nature23646

Hain, M. P., Sigman, D. M., Higgins, J. A., & Haug, G. H. (2015). The effects of secular calcium and magnesium concentration changes on the thermodynamics of seawater acid/base chemistry: Implications for Eocene and Cretaceous ocean carbon chemistry and buffering. *Global Biogeochemical Cycles*, 2014GB004986. https://doi.org/10.1002/2014GB004986

Hansen, J., Sato, M., Russell, G., & Kharecha, P. (2013). Climate sensitivity, sea level and atmospheric carbon dioxide. *Phil. Trans. R. Soc. A*, *371*(2001), 20120294. https://doi.org/10.1098/rsta.2012.0294

Hay, W. W., DeConto, R. M., Wold, C. N., Wilson, K. M., Voigt, S., Schulz, M., et al. (1999). Alternative Global Cretaceous Paleogeography. In E. Barrera & C. C. Johnson (Eds.), *The Evolution of Cretaceous Ocean/Climate Systems* (pp. 1–47). Boulder, CO: Geological Society of America.

Hemming, N. G., & Hanson, G. N. (1992). Boron isotopic composition and concentration in modern marine carbonates. *Geochimica et Cosmochimica Acta*, *56*(1), 537–543. https://doi.org/10.1016/0016-7037(92)90151-8

Henehan, M. J., Rae, J. W. B., Foster, G. L., Erez, J., Prentice, K. C., Kucera, M., et al. (2013). Calibration of the boron isotope proxy in the planktonic foraminifera Globigerinoides ruber for use in palaeo-CO_2 reconstruction. *Earth and Planetary Science Letters*, *364*, 111–122. https://doi.org/10.1016/j.epsl.2012.12.029

Henehan, M. J., Foster, G. L., Bostock, H. C., Greenop, R., Marshall, B. J., & Wilson, P. A. (2016). A new boron isotope-pH calibration for Orbulina universa, with implications for understanding and accounting for 'vital effects.' *Earth and Planetary Science Letters*, *454*, 282–292. https://doi.org/10.1016/j.epsl.2016.09.024

Henehan, M. J., Hull, P. M., Penman, D. E., Rae, J. W. B., & Schmidt, D. N. (2016). Biogeochemical significance of pelagic ecosystem function: an end-Cretaceous case study. *Phil. Trans. R. Soc. B*, *371*(1694), 20150510. https://doi.org/10.1098/rstb.2015.0510

van Hinsbergen, D. J. J., de Groot, L. V., van Schaik, S. J., Spakman, W., Bijl, P. K., Sluijs, A., et al. (2015). A Paleolatitude Calculator for Paleoclimate Studies. *PLOS ONE*, *10*(6), e0126946. https://doi.org/10.1371/journal.pone.0126946

Hönisch, B., Bijma, J., Russell, A. D., Spero, H. J., Palmer, M. R., Zeebe, R. E., & Eisenhauer, A. (2003). The influence of symbiont photosynthesis on the boron isotopic composition of foraminifera shells. *Marine Micropaleontology*, *49*(1–2), 87–96. https://doi.org/10.1016/S0377-8398(03)00030-6

Hönisch, B., Allen, K. A., Lea, D. W., Spero, H. J., Eggins, S. M., Arbuszewski, J., et al. (2013). The influence of salinity on Mg/Ca in planktic foraminifers – Evidence from cultures, core-top sediments and complementary δ18O. *Geochimica et Cosmochimica Acta*, *121*, 196–213. https://doi.org/10.1016/j.gca.2013.07.028

IPCC Core Writing Team. (2014). *Climate Change 2014: Synthesis Report. Contribution of Working Groups I, II and III to the Fifth Assessment Report of the Intergovernmental Panel on Climate Change* (No. AR5) (p. 151 pp). Geneva, Switzerland: IPCC.

Jørgensen, B. B., Erez, J., Revsbech, N. P., & Cohen, Y. (1985). Symbiotic Photosynthesis in a Planktonic Foraminiferan, Globigerinoides sacculifer (Brady), Studied with Microelectrodes. *Limnology and Oceanography*, *30*(6), 1253–1267.

Judd, E. J., Ivany, L. C., DeConto, R. M., Halberstadt, A. R. W., Miklus, N. M., Junium, C. K., & Uveges, B. T. (2019). Seasonally resolved proxy data from the Antarctic Peninsula support a heterogeneous middle Eocene Southern Ocean. *Paleoceanography and Paleoclimatology*. https://doi.org/10.1029/2019PA003581

Katz, M. E., & Miller, K. G. (1991). Early Palaeogene Benthic Foraminiferal Assemblages and Stable Isotopes in the Southern Ocean. In *Proceedings of the Ocean Drilling Program* (Vol. 114, pp. 481–512).

Kelly, D. C., Zachos, J. C., Bralower, T. J., & Schellenberg, S. A. (2005). Enhanced terrestrial weathering/runoff and surface ocean carbonate production during the recovery stages of the Paleocene-Eocene thermal maximum: PETM NEGATIVE FEEDBACK MECHANISMS. *Paleoceanography*, *20*(4), n/a-n/a. https://doi.org/10.1029/2005PA001163

Kennett, J. P., & Stott, L. D. (1991). Abrupt deep-sea warming, palaeoceanographic changes and benthic extinctions at the end of the Palaeocene. *Nature*, *353*(6341), 225–229. https://doi.org/10.1038/353225a0

Kirtland Turner, S., Hull, P. M., Kump, L. R., & Ridgwell, A. (2017). A probabilistic assessment of the rapidity of PETM onset. *Nature Communications*, *8*(1). https://doi.org/10.1038/s41467-017-00292-2

Koch, P. L., Zachos, J. C., & Gingerich, P. D. (1992). Correlation between isotope records in marine and continental carbon reservoirs near the Palaeocene/Eocene boundary. *Nature*, *358*(6384), 319–322. https://doi.org/10.1038/358319a0

Kocken, I. J., Cramwinckel, M. J., Zeebe, R. E., Middelburg, J. J., & Sluijs, A. (2019). The 405 kyr and 2.4 Myr eccentricity components in Cenozoic carbon isotope records. *Climate of the Past*, *15*(1), 91–104. https://doi.org/10.5194/cp-15-91-2019

Köhler-Rink, S., & Kühl, M. (2005). The chemical microenvironment of the symbiotic planktonic foraminifer Orbulina universa. *Marine Biology Research*, *1*(1), 68–78. https://doi.org/10.1080/17451000510019015

Kominz, M. A., Browning, J. V., Miller, K. G., Sugarman, P. J., Mizintseva, S., & Scotese, C. R. (2008). Late Cretaceous to Miocene sea-level estimates from the New Jersey and Delaware coastal plain coreholes: an error analysis. *Basin Research*, *20*(2), 211–226. https://doi.org/10.1111/j.1365-2117.2008.00354.x

Lear, C. H. (2000). Cenozoic Deep-Sea Temperatures and Global Ice Volumes from Mg/Ca in Benthic Foraminiferal Calcite. *Science*, *287*(5451), 269–272. https://doi.org/10.1126/science.287.5451.269

Liu, R. Y. (1988). Bootstrap procedures under some non-iid models. *The Annals of Statistics*, *16*(4), 1696–1708.

Lyle, M. W., Olivarez, A., Backman, J., & Tripati, A. K. (2005). Biogenic Sedimentation in the Eocene Equatorial Pacific-The Stuttering Greenhouse and Eocene Carbonate Compensation Depth. In P. A. Wilson, M. Lyle, & J. V. Firth (Eds.), *Proceedings of the Ocean Drilling Program, 199 Scientific Results* (Vol. 199, pp. 1-35 [Online]). Ocean Drilling Program. Retrieved from http://www-odp.tamu.edu/publications/199_SR/199TOC.HTM

Mammen, E. (1993). Bootstrap and Wild Bootstrap for High Dimensional Linear Models. *The Annals of Statistics*, *21*(1), 255–285.

Margolis, S. V., & Kennett, J. P. (1970). Antarctic Glaciation during the Tertiary Recorded in Sub-Antarctic Deep-Sea Cores. *Science*, *170*(3962), 1085–1087. https://doi.org/10.1126/science.170.3962.1085

Martínez-Botí, M. A., Marino, G., Foster, G. L., Ziveri, P., Henehan, M. J., Rae, J. W. B., et al. (2015). Boron isotope evidence for oceanic carbon dioxide leakage during the last deglaciation. *Nature*, *518*(7538), 219–222. https://doi.org/10.1038/nature14155

Millero, F. J., & Pierrot, D. (1998). A Chemical Equilibrium Model for Natural Waters. *Aquatic Geochemistry*, *4*(1), 153–199. https://doi.org/10.1023/A:1009656023546

Misra, S., & Froelich, P. N. (2012). Lithium Isotope History of Cenozoic Seawater: Changes in Silicate Weathering and Reverse Weathering. *Science*, *335*(6070), 818–823. https://doi.org/10.1126/science.1214697

Moebius, I., Friedrich, O., Edgar, K. M., & Sexton, P. F. (2015). Episodes of intensified biological productivity in the subtropical Atlantic Ocean during the termination of the Middle Eocene Climatic Optimum (MECO): Intensified Productivity during the MECO. *Paleoceanography*, n/a-n/a. https://doi.org/10.1002/2014PA002673

Moore, T. C., Jarrard, R. D., Olivarez Lyle, A., & Lyle, M. (2008). Eocene biogenic silica accumulation rates at the Pacific equatorial divergence zone. *Paleoceanography*, *23*(2), n/a-n/a. https://doi.org/10.1029/2007PA001514

Myhre, G., Highwood, E., Shine, K., & Stordal, F. (1998). New estimates of radiative forcing due to well mixed greenhouse gases. *Geophysical Research Letters*, *25*(14), 2715–2718.

Norris, R. D., Wilson, D., Blum, P., & the Expedition 342 Scientists (Eds.). (2014). *Proceedings of the Integrated Ocean Drilling Program, 342 Initial Reports* (Vol. 342). College Station, TX: Ocean Drilling Program. Retrieved from http://publications.iodp.org/proceedings/342/342title.htm

Okai, T., Suzuki, A., Kawahata, H., Terashima, S., & Imai, N. (2002). Preparation of a New Geological Survey of Japan Geochemical Reference Material: Coral JCp-1. *Geostandards Newsletter*, *26*(1), 95–99. https://doi.org/10.1111/j.1751-908X.2002.tb00627.x

Pälike, H., Lyle, M. W., Nishi, H., Raffi, I., Ridgwell, A., Gamage, K., et al. (2012). A Cenozoic record of the equatorial Pacific carbonate compensation depth. *Nature*, *488*(7413), 609–614. https://doi.org/10.1038/nature11360

Pearson, P. N., & Palmer, M. R. (1999). Middle Eocene Seawater pH and Atmospheric Carbon Dioxide Concentrations. *Science*, *284*(5421), 1824–1826. https://doi.org/10.1126/science.284.5421.1824

Pearson, P. N., & Palmer, M. R. (2000). Atmospheric carbon dioxide concentrations over the past 60 million years. *Nature*, *406*(6797), 695–699. https://doi.org/10.1038/35021000

Pearson, P. N., Shackleton, N. J., & Hall, M. A. (1993). Stable isotope paleoecology of middle Eocene planktonic foraminifera and multi-species isotope stratigraphy, DSDP Site 523, South Atlantic. *The Journal of Foraminiferal Research*, *23*(2), 123–140. https://doi.org/10.2113/gsjfr.23.2.123

Pearson, P. N., Ditchfield, P. W., Singano, J., Harcourt-Brown, K. G., Nicholas, C. J., Olsson, R. K., et al. (2001). Warm tropical sea surface temperatures in the Late Cretaceous and Eocene epochs. *Nature*, *413*(6855), 481–487. https://doi.org/10.1038/35097000

Pearson, P. N., Olsson, R. K., Huber, B. T., Hemleben, C., & Berggren, W. A. (Eds.). (2006). *Atlas of Eocene planktonic foraminifera*. Cushman Foundation.

Pearson, P. N., Foster, G. L., & Wade, B. S. (2009). Atmospheric carbon dioxide through the Eocene–Oligocene climate transition. *Nature*, *461*(7267), 1110–1113. https://doi.org/10.1038/nature08447

Pekar, S. F., Hucks, A., Fuller, M., & Li, S. (2005). Glacioeustatic changes in the early and middle Eocene (51–42 Ma): Shallow-water stratigraphy from ODP Leg 189 Site 1171 (South Tasman Rise) and deep-sea δ18O records. *Geological Society of America Bulletin*, *117*(7), 1081. https://doi.org/10.1130/B25486.1

Penman, D. E. (2016). Silicate weathering and North Atlantic silica burial during the Paleocene-Eocene Thermal Maximum. *Geology*, *44*(9), 731–734. https://doi.org/10.1130/G37704.1

Penman, D. E., & Zachos, J. C. (2018). New constraints on massive carbon release and recovery processes during the Paleocene-Eocene Thermal Maximum. *Environmental Research Letters*, *13*(10), 105008. https://doi.org/10.1088/1748-9326/aae285

Penman, D. E., Turner, S. K., Sexton, P. F., Norris, R. D., Dickson, A. J., Boulila, S., et al. (2016). An abyssal carbonate compensation depth overshoot in the aftermath of the Palaeocene–Eocene Thermal Maximum. *Nature Geoscience*, *9*(8), 575–580. https://doi.org/10.1038/ngeo2757

Penman, D. E., Keller, A., D'haenens, S., Kirtland Turner, S., & Hull, P. M. (2019). Atlantic Deep-Sea Cherts Associated With Eocene Hyperthermal Events. *Paleoceanography and Paleoclimatology*, *34*(2), 287–299. https://doi.org/10.1029/2018PA003503

Pisias, N. G., & Mix, A. C. (1988). Aliasing of the geological record and the search for long-period Milankovitch Cycles. *Paleoceanography*, *3*(5), 613–619.

van der Ploeg, R., Selby, D., Cramwinckel, M. J., Li, Y., Bohaty, S. M., Middelburg, J. J., & Sluijs, A. (2018). Middle Eocene greenhouse warming facilitated by diminished weathering feedback. *Nature Communications*, *9*(1). https://doi.org/10.1038/s41467-018-05104-9

Pomar, L., Baceta, J. I., Hallock, P., Mateu-Vicens, G., & Basso, D. (2017). Reef building and carbonate production modes in the west-central Tethys during the Cenozoic. *Marine and Petroleum Geology*, *83*, 261–304. https://doi.org/10.1016/j.marpetgeo.2017.03.015

Premoli Silva, I., Wade, B. S., & Pearson, P. N. (2006). Taxonomy of Globigerinatheka and Orbulinoides. In P. N. Pearson, R. K. Olsson, B. T. Huber, C. Hemleben, & W. A. Berggren (Eds.), *Atlas of Eocene Planktonic Foraminifera* (pp. 461–508). Fredericksburg, VA: Cushman Foundation.

R Core Team. (2015). *R: A language and environment for statistical computing.* Vienna, Austria: R Foundation for Statistical Computing. Retrieved from www.R-project.org

Rae, J. W. B., Foster, G. L., Schmidt, D. N., & Elliott, T. (2011). Boron isotopes and B/Ca in benthic foraminifera: Proxies for the deep ocean carbonate system. *Earth and Planetary Science Letters*, *302*(3–4), 403–413. https://doi.org/10.1016/j.epsl.2010.12.034

Roberts, J., Kaczmarek, K., Langer, G., Skinner, L. C., Bijma, J., Bradbury, H., et al. (2018). Lithium isotopic composition of benthic foraminifera: A new proxy for paleo-pH reconstruction. *Geochimica et Cosmochimica Acta*, *236*, 336–350. https://doi.org/10.1016/j.gca.2018.02.038

Rohling, E., & Members, P. P. (2012). Making sense of palaeoclimate sensitivity. *Nature*, *491*(7426), 683–691. https://doi.org/10.1038/nature11574

Rose, K. C., Ferraccioli, F., Jamieson, S. S. R., Bell, R. E., Corr, H., Creyts, T. T., et al. (2013). Early East Antarctic Ice Sheet growth recorded in the landscape of the Gamburtsev Subglacial Mountains. *Earth and Planetary Science Letters*, *375*, 1–12. https://doi.org/10.1016/j.epsl.2013.03.053

Sauermilch, I., Whittaker, J. M., Bijl, P. K., Totterdell, J. M., & Jokat, W. (2019). Tectonic, Oceanographic, and Climatic Controls on the Cretaceous-Cenozoic Sedimentary Record of the Australian-Antarctic Basin. *Journal of Geophysical Research: Solid Earth*. https://doi.org/10.1029/2018JB016683

Savian, J. F., Jovane, L., Giorgioni, M., Iacoviello, F., Rodelli, D., Roberts, A. P., et al. (2016). Environmental magnetic implications of magnetofossil occurrence during the Middle Eocene Climatic Optimum (MECO) in pelagic sediments from the equatorial Indian Ocean.

Palaeogeography, Palaeoclimatology, Palaeoecology, *441*, 212–222. https://doi.org/10.1016/j.palaeo.2015.06.029

Scher, H. D., & Delaney, M. L. (2010). Breaking the glass ceiling for high resolution Nd isotope records in early Cenozoic paleoceanography. *Chemical Geology*, *269*(3–4), 329–338. https://doi.org/10.1016/j.chemgeo.2009.10.007

Scher, H. D., Bohaty, S. M., Smith, B. W., & Munn, G. H. (2014). Isotopic interrogation of a suspected late Eocene glaciation: hidden glaciation revealed in the Eocene. *Paleoceanography*, *29*(6), 628–644. https://doi.org/10.1002/2014PA002648

Sexton, P. F., Wilson, P. A., & Pearson, P. N. (2006a). Microstructural and geochemical perspectives on planktic foraminiferal preservation: "Glassy" versus "Frosty." *Geochemistry, Geophysics, Geosystems*, *7*(12), Q12P19. https://doi.org/10.1029/2006GC001291

Sexton, P. F., Wilson, P. A., & Pearson, P. N. (2006b). Palaeoecology of late middle Eocene planktic foraminifera and evolutionary implications. *Marine Micropaleontology*, *60*(1), 1–16. https://doi.org/10.1016/j.marmicro.2006.02.006

Sexton, P. F., Wilson, P. A., & Norris, R. D. (2006). Testing the Cenozoic multisite composite δ^{18}O and δ^{13}C curves: New monospecific Eocene records from a single locality, Demerara Rise (Ocean Drilling Program Leg 207). *Paleoceanography*, *21*(2), PA2019. https://doi.org/10.1029/2005PA001253

Sexton, P. F., Norris, R. D., Wilson, P. A., Pälike, H., Westerhold, T., Röhl, U., et al. (2011). Eocene global warming events driven by ventilation of oceanic dissolved organic carbon. *Nature*, *471*(7338), 349–352. https://doi.org/10.1038/nature09826

Shipboard Scientific Party. (1988). Site 702. In P. F. Ciesielski, Y. Kristoffersen, & et al. (Eds.), *Proceedings of the Ocean Drilling Program, 114 Initial Reports* (Vol. 114, pp. 483–548). College Station, TX: Ocean Drilling Program. Retrieved from http://www-odp.tamu.edu/publications/114_IR/114TOC.HTM

Shipboard Scientific Party. (2004a). Site 1260. In J. Erbacher, D. C. Mosher, M. J. Malone, & et al. (Eds.), *Proceedings of the Ocean Drilling Program, 207 Initial Reports* (Vol. 207, pp. 1–113). Ocean Drilling Program. https://doi.org/10.2973/odp.proc.ir.207.107.2004

Shipboard Scientific Party. (2004b). Site 1263. In J.C. Zachos, D. Kroon, P. Blum, & et al. (Eds.), *Proceedings of the Ocean Drilling Program, 208 Initial Reports* (Vol. 208, pp. 1–87). Ocean Drilling Program. https://doi.org/10.2973/odp.proc.ir.208.104.2004

Sluijs, A., Zeebe, R. E., Bijl, P. K., & Bohaty, S. M. (2013). A middle Eocene carbon cycle conundrum. *Nature Geoscience*, *6*(6), 429–434. https://doi.org/10.1038/ngeo1807

Sømme, T. O., Helland-Hansen, W. & Granjeon, D. (2009). Impact of eustatic amplitude variations on shelf morphology, sediment dispersal, and sequence stratigraphic interpretation: Icehouse versus greenhouse systems. *Geology*, 37(7), 587-590. https://doi.org/10.1130/G25511A.1.

Spero, H. J., Lerche, I., & Williams, D. F. (1991). Opening the carbon isotope "vital effect" black box, 2, Quantitative model for interpreting foraminiferal carbon isotope data. *Paleoceanography*, *6*(6), 639–655. https://doi.org/10.1029/91PA02022

Spofforth, D. J. A., Agnini, C., Pälike, H., Rio, D., Fornaciari, E., Giusberti, L., et al. (2010). Organic carbon burial following the middle Eocene climatic optimum in the central western Tethys. *Paleoceanography*, *25*(3). https://doi.org/10.1029/2009PA001738

Stickley, C. E., St John, K., Koç, N., Jordan, R. W., Passchier, S., Pearce, R. B., & Kearns, L. E. (2009). Evidence for middle Eocene Arctic sea ice from diatoms and ice-rafted debris. *Nature*, *460*(7253), 376–379. https://doi.org/10.1038/nature08163

Storey, M., Duncan, R. A., & Swisher, C. C. (2007). Paleocene-Eocene Thermal Maximum and the Opening of the Northeast Atlantic. *Science*, *316*(5824), 587–589. https://doi.org/10.1126/science.1135274

Svensen, H., Planke, S., Malthe-Sørenssen, A., Jamtveit, B., Myklebust, R., Rasmussen Eidem, T., & Rey, S. S. (2004). Release of methane from a volcanic basin as a mechanism for initial Eocene global warming. *Nature*, *429*(6991), 542–545. https://doi.org/10.1038/nature02566

Torres, M. A., Moosdorf, N., Hartmann, J., Adkins, J. F., & West, A. J. (2017). Glacial weathering, sulfide oxidation, and global carbon cycle feedbacks. *Proceedings of the National Academy of Sciences*, *114*(33), 8716–8721. https://doi.org/10.1073/pnas.1702953114

Tripati, A. K., Backman, J., Elderfield, H., & Ferretti, P. (2005). Eocene bipolar glaciation associated with global carbon cycle changes. *Nature*, *436*(7049), 341–346. https://doi.org/10.1038/nature03874

Tripati, A. K., Eagle, R. A., Morton, A., Dowdeswell, J. A., Atkinson, K. L., Bahé, Y., et al. (2008). Evidence for glaciation in the Northern Hemisphere back to 44 Ma from ice-rafted debris in the Greenland Sea. *Earth and Planetary Science Letters*, *265*(1–2), 112–122. https://doi.org/10.1016/j.epsl.2007.09.045

Vahlenkamp, M., Niezgodzki, I., De Vleeschouwer, D., Bickert, T., Harper, D., Kirtland Turner, S., et al. (2018). Astronomically paced changes in deep-water circulation in the western North Atlantic during the middle Eocene. *Earth and Planetary Science Letters*, *484*, 329–340. https://doi.org/10.1016/j.epsl.2017.12.016

Vigier, N., & Goddéris, Y. (2015). A new approach for modeling Cenozoic oceanic lithium isotope paleo-variations: the key role of climate. *Climate of the Past*, *11*(4), 635–645. https://doi.org/10.5194/cp-11-635-2015

Vigier, N., Rollion-Bard, C., Levenson, Y., & Erez, J. (2015). Lithium isotopes in foraminifera shells as a novel proxy for the ocean dissolved inorganic carbon (DIC). *Comptes Rendus Geoscience*, *347*(1), 43–51. https://doi.org/10.1016/j.crte.2014.12.001

Wade, B. S., Al-Sabouni, N., Hemleben, C., & Kroon, D. (2008). Symbiont bleaching in fossil planktonic foraminifera. *Evolutionary Ecology*, *22*(2), 253–265.

Westerhold, Thomas, & Röhl, U. (2013). Orbital pacing of Eocene climate during the Middle Eocene Climate Optimum and the chron C19r event: Missing link found in the tropical western Atlantic: Orbital Pacing of Eocene Climate. *Geochemistry, Geophysics, Geosystems*, *14*(11), 4811–4825. https://doi.org/10.1002/ggge.20293

Westerhold, Thomas, Röhl, U., Pälike, H., Wilkens, R., Wilson, P. A., & Acton, G. (2014). Orbitally tuned timescale and astronomical forcing in the middle Eocene to early Oligocene. *Climate of the Past*, *10*(3), 955–973. https://doi.org/10.5194/cp-10-955-2014

Westerhold, Thomas, Röhl, U., Donner, B., & Zachos, J. C. (2018). Global Extent of Early Eocene Hyperthermal Events: A New Pacific Benthic Foraminiferal Isotope Record From Shatsky Rise (ODP Site 1209). *Paleoceanography and Paleoclimatology*, *33*(6), 626–642. https://doi.org/10.1029/2017PA003306

Westerhold, Thomas, Röhl, U., Donner, B., Frederichs, T., Kordesch, W. E. C., Bohaty, S. M., et al. (2018). Late Lutetian Thermal Maximum-Crossing a Thermal Threshold in Earth's Climate System? *Geochemistry, Geophysics, Geosystems*, *19*(1), 73–82. https://doi.org/10.1002/2017GC007240

Witkowski, J., Bohaty, S. M., McCartney, K., & Harwood, D. M. (2012). Enhanced siliceous plankton productivity in response to middle Eocene warming at Southern Ocean ODP Sites 748 and 749. *Palaeogeography, Palaeoclimatology, Palaeoecology*, *326–328*, 78–94. https://doi.org/10.1016/j.palaeo.2012.02.006

Witkowski, J., Bohaty, S. M., Edgar, K. M., & Harwood, D. M. (2014). Rapid fluctuations in mid-latitude siliceous plankton production during the Middle Eocene Climatic Optimum (ODP Site 1051, western North Atlantic). *Marine Micropaleontology*, *106*, 110–129. https://doi.org/10.1016/j.marmicro.2014.01.001

Zachos, James C., Rohl, U., Schellenberg, S. A., Sluijs, A., Hodell, D. A., Kelly, D. C., et al. (2005). Rapid Acidification of the Ocean During the Paleocene-Eocene Thermal Maximum. *Science*, *308*(5728), 1611–1615. https://doi.org/10.1126/science.1109004

Zeebe, R. E. (2012). LOSCAR: Long-term Ocean-atmosphere-Sediment CArbon cycle Reservoir Model v2.0.4. *Geosci. Model Dev.*, *5*(1), 149–166. https://doi.org/10.5194/gmd-5-149-2012

Zeebe, R. E., & Wolf-Gladrow, D. A. (2001). *CO2 in seawater: Equilibrium, Kinetics, Isotopes.* Amsterdam: Elsevier.

Zeebe, R. E., Wolf-Gladrow, D. A., Bijma, J., & Hönisch, B. (2003). Vital effects in foraminifera do not compromise the use of δ^{11}B as a paleo-*p*H indicator: Evidence from modeling: CRETACEOUS MARINE TEMPERATURE EVOLUTION. *Paleoceanography*, *18*(2), n/a-n/a. https://doi.org/10.1029/2003PA000881

Supporting Figures

Figure S1. *Stratigraphic tie points between our four studied core sites. Magnetic stratigraphy from ODP Site 702 is translated to each other site according to recognizable features in oxygen (O1-9; blue squares) and carbon (C1-9; green squares) isotope records. For further description of these tie points see table S1. Magnetochron boundaries are shown as yellow stars, and biostratigraphic horizons (where used) are shown as pink stars.*

Figure S2. *Testing body size-$\delta^{13}C$ gradients for evidence of 'bleaching' in* A. praetopilensis *and* M. crassatus *at ODP Sites 1260 (left, panels **a**, **c**, **e**) and 865 (right, panels **b**, **d**, **f**). At both sites, the symbiont-barren, deeper-dwelling species* S. linaperta *is shown for comparison. Analysed samples are as follows: **a**) 1260A-8R-2, 77-78.5 cm, **b**) 865C-5H-3, 25-27 cm, **c**) 1260A-6R-4, 77-78.5 cm, **d**) 865C-5H-1, 5-7 cm, **e**) 1260A-6R-1, 7-8.5 cm, and **f**) 865C-4H-6, 25-27 cm. No site or time-slice shows a collapse in $\delta^{13}C$ gradient indicative of bleaching.*

Figure S3*. Mg/Ca-derived temperatures (assuming $[Mg]_{sw}$ = 38 mM, $[Ca]_{sw}$ = 17 mM) for our study sites, without (left, panel **a**) and with (right, panel **b**) pH corrections (Evans, Wade, et al., 2016) based on $\delta^{11}B$. Not correcting for pH change can result in significant overestimation of temperature of almost 5 ℃. Note for the purposes of visual representation in panel b, we use boron-derived pH reconstructions from our four sites species-specific calibrations. Note these pH calculations assume $\delta^{11}B_{sw}$ of 38.5-38.9 ‰, $[Mg]_{sw}$= 38 mM, and $[Ca]_{sw}$= 17 mM, and temperature estimates from Mg/Ca (see Section 4). Error bars on temperature estimates in panel **a** are 2 standard deviations of 1,000 Monte Carlo simulations, incorporating 3% uncertainty in measured Mg/Ca ratios and ±3 mM uncertainty on each major ion concentration. Error bars in panel **b** are again 2 standard deviations of 1,000 Monte Carlo simulations with the uncertainties of panel **a**, but in addition simulations incorporate ±0.2‰ uncertainty on $\delta^{11}B_{sw}$ and measurement uncertainty on $\delta^{11}B$. The main sources of uncertainty are systematic throughout the record, with Mg/Ca_{sw} inflating uncertainty particularly strongly. To better illustrate internal consistency within records, in panel **b** colored error bars denote the uncertainty stemming only from measurement uncertainty in Mg/Ca and $\delta^{11}B$. Paleolatitude estimates plotted on panel **b** are from (van Hinsbergen et al., 2015).*

Figure S4. *Boron-derived pH reconstructions from the four study sites with vital effect calibrations for all species (**a**) and only applying species-specific calibrations to* Globigerinatheka kugleri *and* Globigerinatheka index *(**b**). Note these calculations assume $\delta^{11}B_{sw}$ of 38.7 ‰, $[Mg]_{sw}$= 38 mM, and $[Ca]_{sw}$= 17 mM, and temperature estimates from planktic foraminiferal Mg/Ca (see Section 2.5).*

Figure S5*. To ascertain whether trends in pH prior to the peak MECO were statistically significant, we compare regressions through each dataset. Confidence intervals (1 and 2σ) on the regressions are calculated using a Monte Carlo approach, from the distributions of 1,000 regression lines plotted through replicate datasets randomly subsampled from within the range of uncertainty in pH for each datapoint. The regression lines themselves are calculated via a wild bootstrap approach (Liu, 1988; Mammen, 1993), which avoids problems that can arise when utilizing traditional bootstrap re-sampling on small datasets (Cameron et al., 2008). In each plot, the regression lines from one site (bold colored lines) are compared to other sites (thinner colored lines) and to a slope of zero (i.e. no change; black dashed line). No site produced a trend over time that is outside of uncertainty of a slope of 0. While it would be preferable to look at the MECO onset interval (40.21 – 40.5 Ma) in isolation, for some sites this would leave only 2 – 3 datapoints, and hence would result in artificially-inflated uncertainty bounds. Note that for this exercise we assume $\delta^{11}B_{sw}$ between 38.5 and 38.9 ‰.*

***Figure S6**. The 1 and 2 se bounds of uncertainty from 500 Monte Carlo-simulated LOESS fits at $\delta^{11}B_{sw}$ = 38.7 ± 0.2‰. For 'pre-event' pH, values shown are the average of the datapoints in our time series in Fig. 2 before the main pH excursion begins, and 2sd of this mean. For 'peak event' pH, the range of uncertainty is that shown around the minimum value of our LOESS fit in Fig. 2. LOSCAR was spun up to each 'pre-event' value to calculate pCO_2. For peak pCO_2 values, iterative carbon additions were added to the mean pre-event pH scenario until LOSCAR reached the desired peak event surface pH value, and resultant pCO_2 noted.*

***Figure S7**. The distribution of ΔpCO_2 in 1,000 simulated datasets over the MECO onset interval, when alkalinity is held constant at 1750±150 µmol/kg. Also plotted are the mean, and 1, 2, and 3 standard deviations around the mean. While a small CO_2 rise is the most likely scenario over this onset interval, the magnitude was unlikely to be large. Note that in this scenario ($\delta^{11}B_{sw}$= 38.5-38.9 ‰), pre-event pCO_2 was ~550 µatm, meaning that even at the upper end of the scale, pCO_2 increase during the onset interval was likely a fraction of a doubling.*

Figure 1.

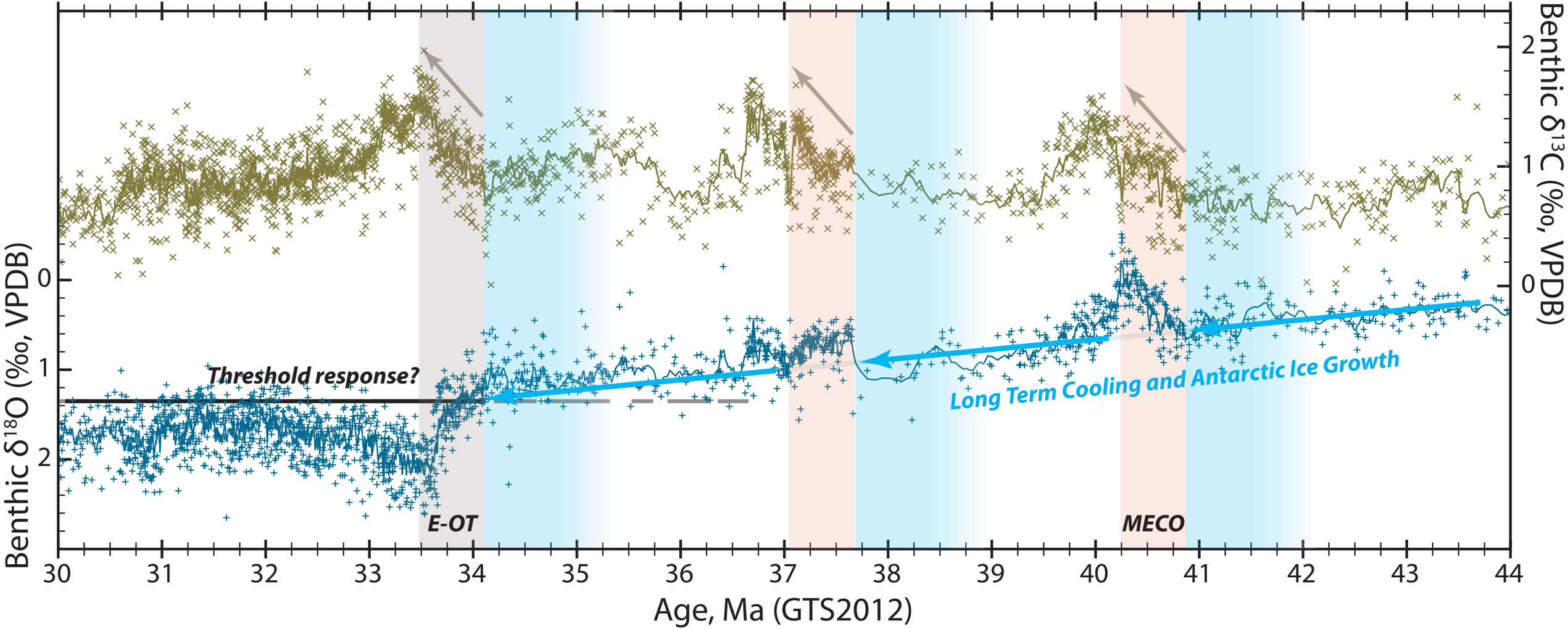
Benthic δ18O (‰, VPDB)
Benthic δ13C (‰, VPDB)
Age, Ma (GTS2012)
Threshold response?
E-OT
MECO
Long Term Cooling and Antarctic Ice Growth
0
1
2
30
31
32
33
34
35
36
37
38
39
40
41
42
43
44

Figure 2.

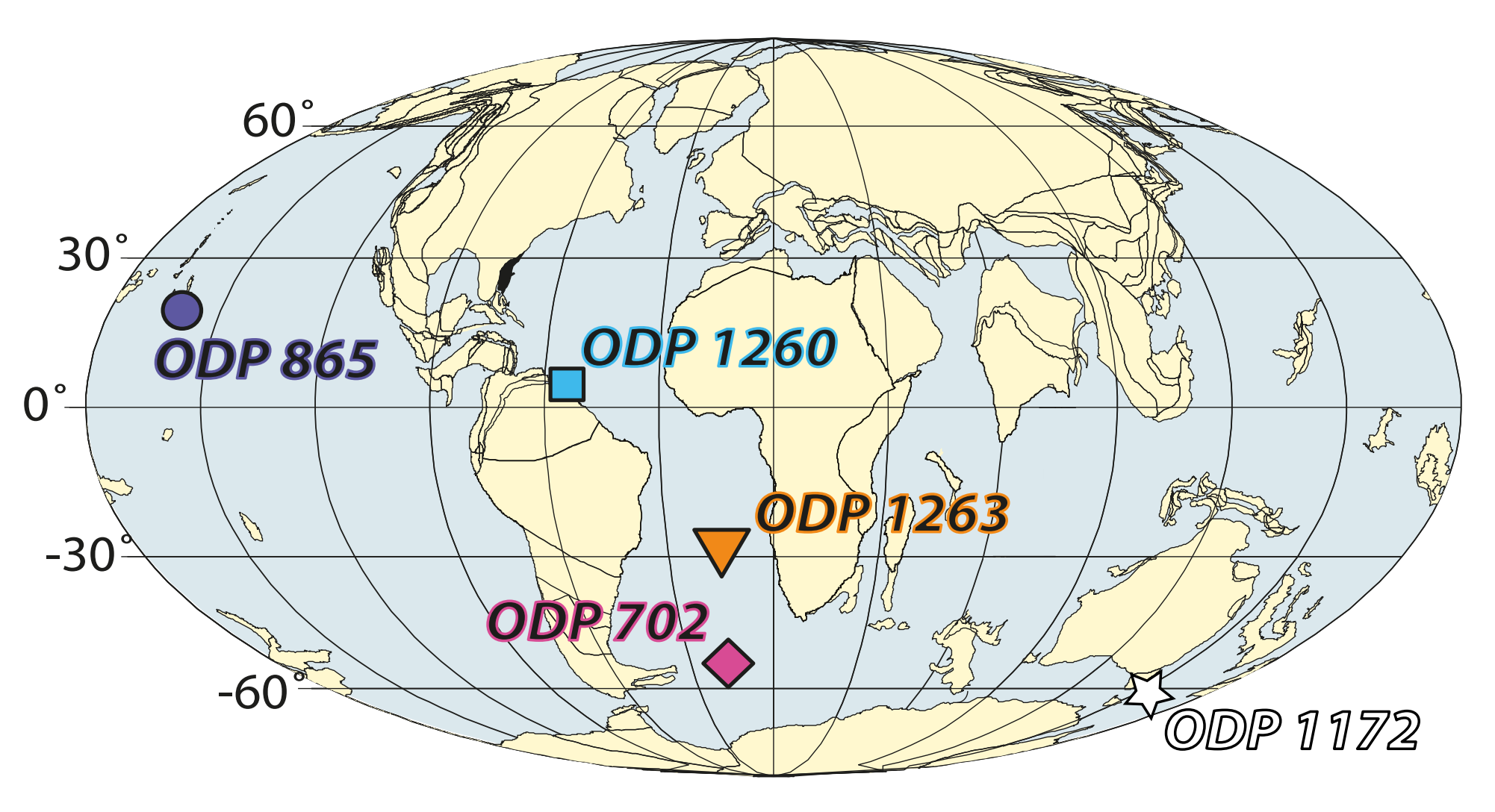
60°
30°
0°
-30°
-60°
ODP 865
ODP 1260
ODP 1263
ODP 702
ODP 1172

Figure 3.

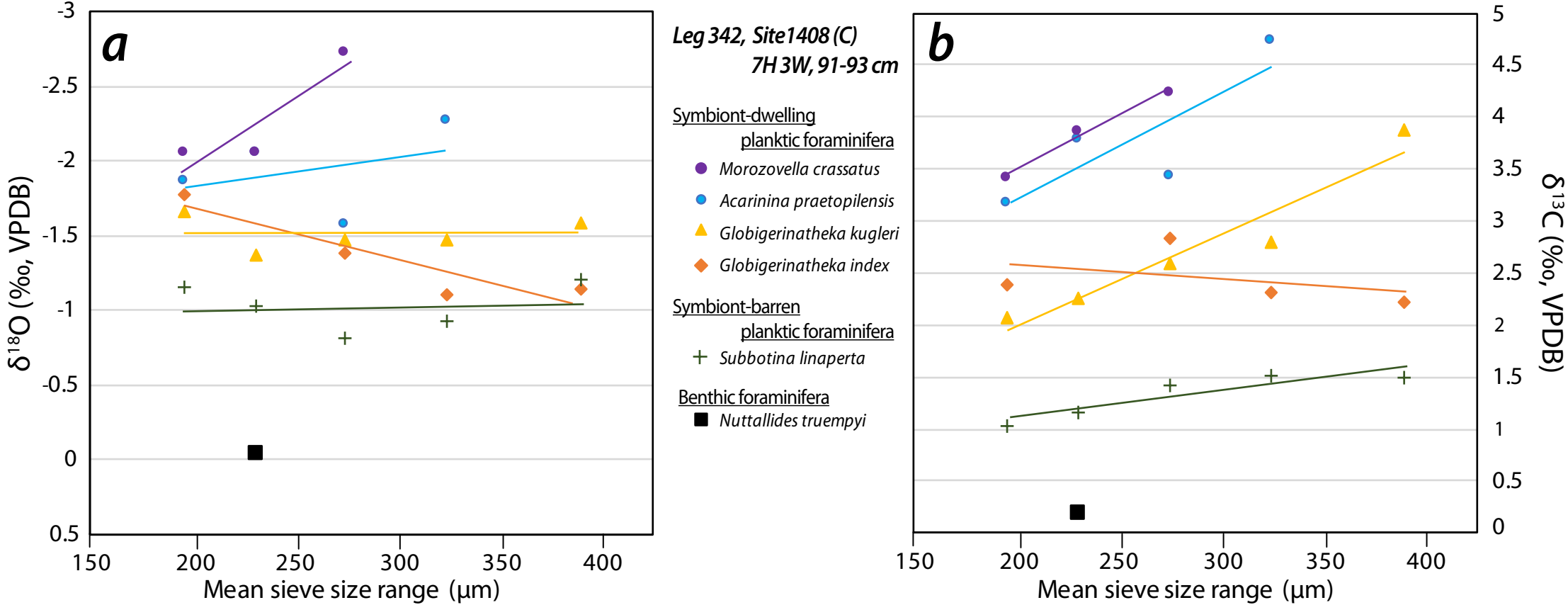
a
b
Leg 342, Site1408 (C)
7H 3W, 91-93 cm
Symbiont-dwelling planktic foraminifera
Morozovella crassatus
Acarinina praetopilensis
Globigerinatheka kugleri
Globigerinatheka index
Symbiont-barren planktic foraminifera
Subbotina linaperta
Benthic foraminifera
Nuttallides truempyi
δ18O (‰, VPDB)
δ13C (‰, VPDB)
Mean sieve size range (µm)
Mean sieve size range (µm)
-3
-2.5
-2
-1.5
-1
-0.5
0
0.5
5
4.5
4
3.5
3
2.5
2
1.5
1
0.5
0
150
200
250
300
350
400

Figure 4.

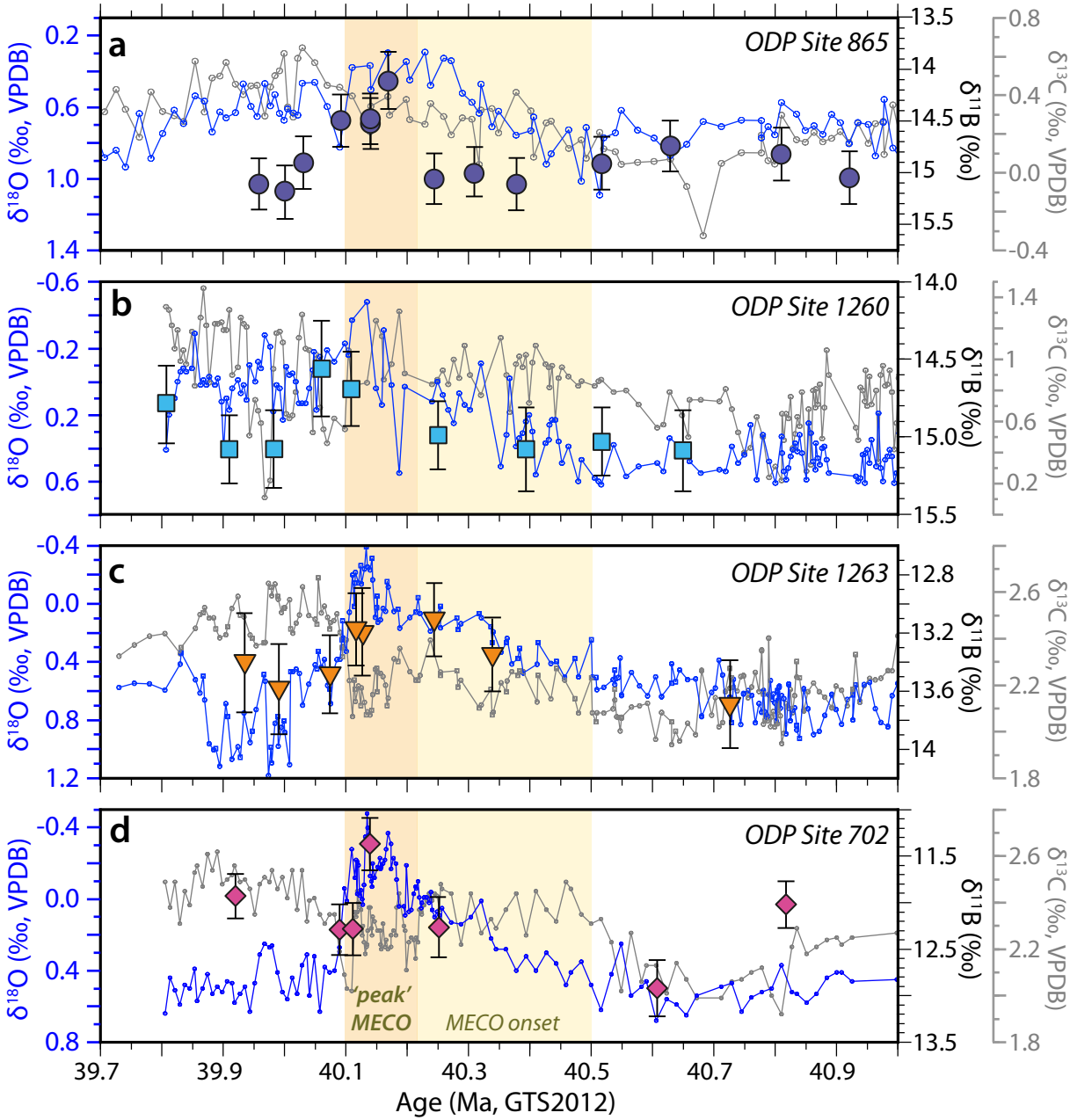
a
ODP Site 865
b
ODP Site 1260
c
ODP Site 1263
d
ODP Site 702
δ18O (‰, VPDB)
δ11B (‰)
δ13C (‰, VPDB)
'peak' MECO
MECO onset
39.7
39.9
40.1
40.3
40.5
40.7
40.9
Age (Ma, GTS2012)

Figure 5.

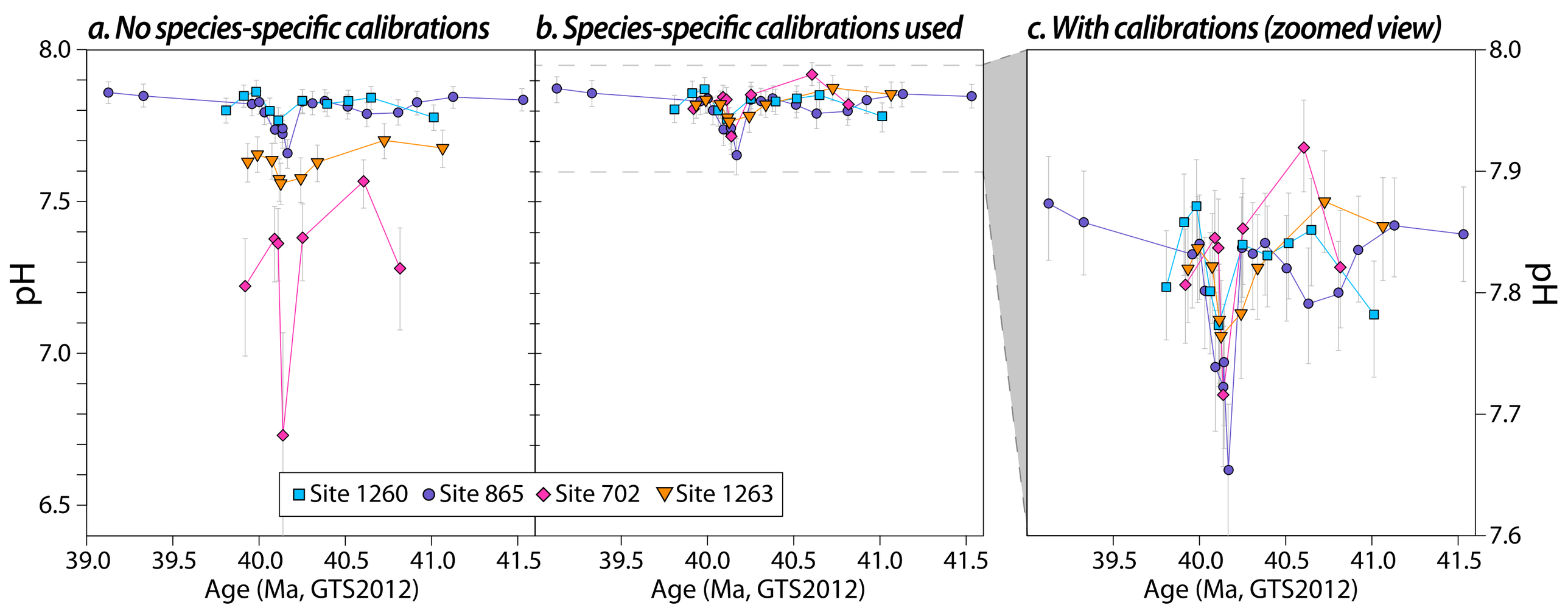
a. No species-specific calibrations
b. Species-specific calibrations used
c. With calibrations (zoomed view)
pH
Age (Ma, GTS2012)
Site 1260
Site 865
Site 702
Site 1263
8.0
7.5
7.0
6.5
7.9
7.8
7.7
7.6
39.0
39.5
40.0
40.5
41.0
41.5

Figure 6.

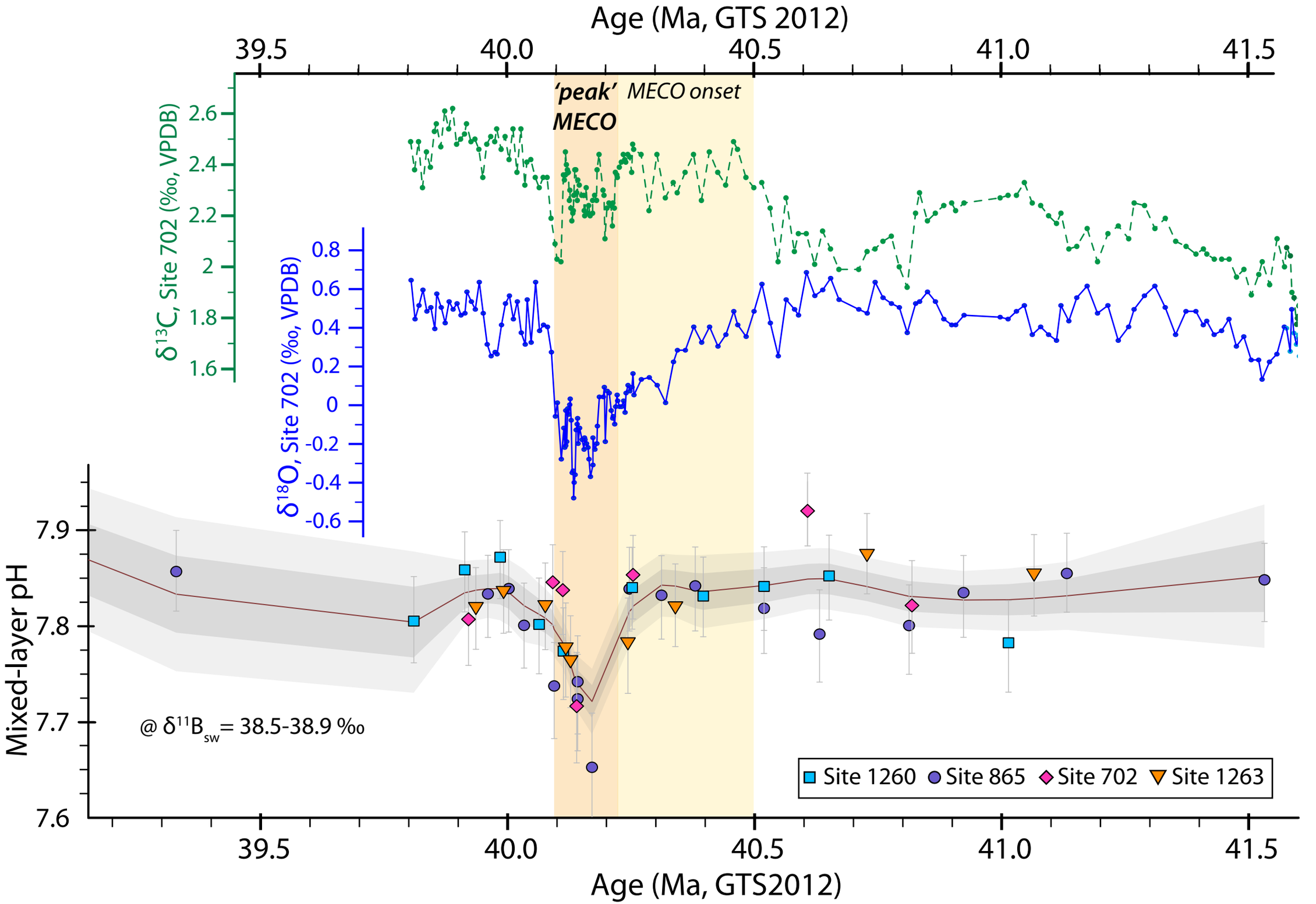
Age (Ma, GTS 2012)
39.5
40.0
40.5
41.0
41.5
'peak' MECO
MECO onset
δ13C, Site 702 (‰, VPDB)
2.6
2.4
2.2
2
1.8
1.6
δ18O, Site 702 (‰, VPDB)
0.8
0.6
0.4
0.2
0
-0.2
-0.4
-0.6
Mixed-layer pH
7.9
7.8
7.7
7.6
@ δ11Bsw = 38.5-38.9 ‰
Site 1260
Site 865
Site 702
Site 1263
Age (Ma, GTS2012)

Figure 7.

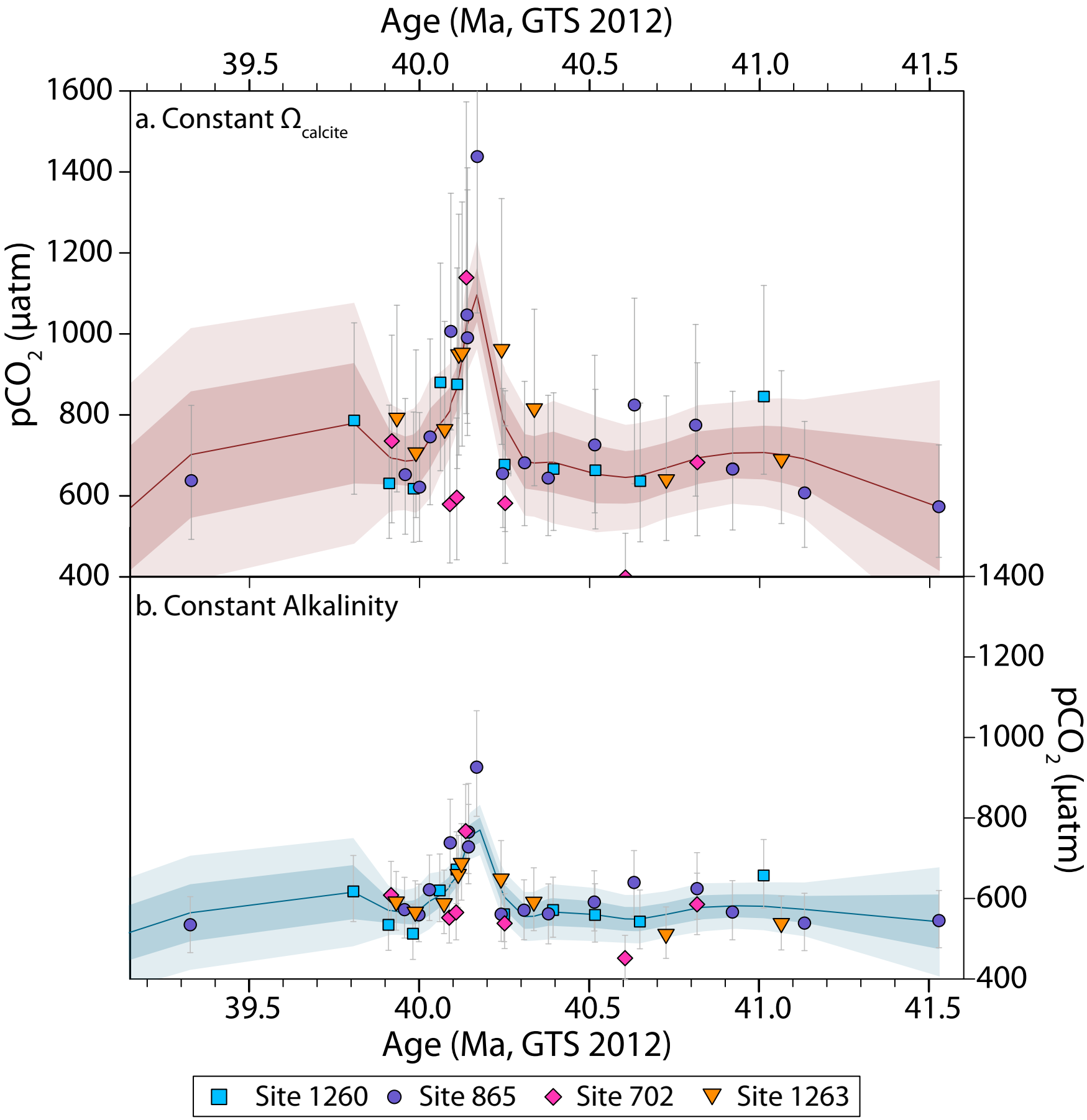
Age (Ma, GTS 2012)
39.5
40.0
40.5
41.0
41.5
a. Constant Ω calcite
b. Constant Alkalinity
pCO2 (µatm)
1600
1400
1200
1000
800
600
400
Site 1260
Site 865
Site 702
Site 1263

Figure 8.

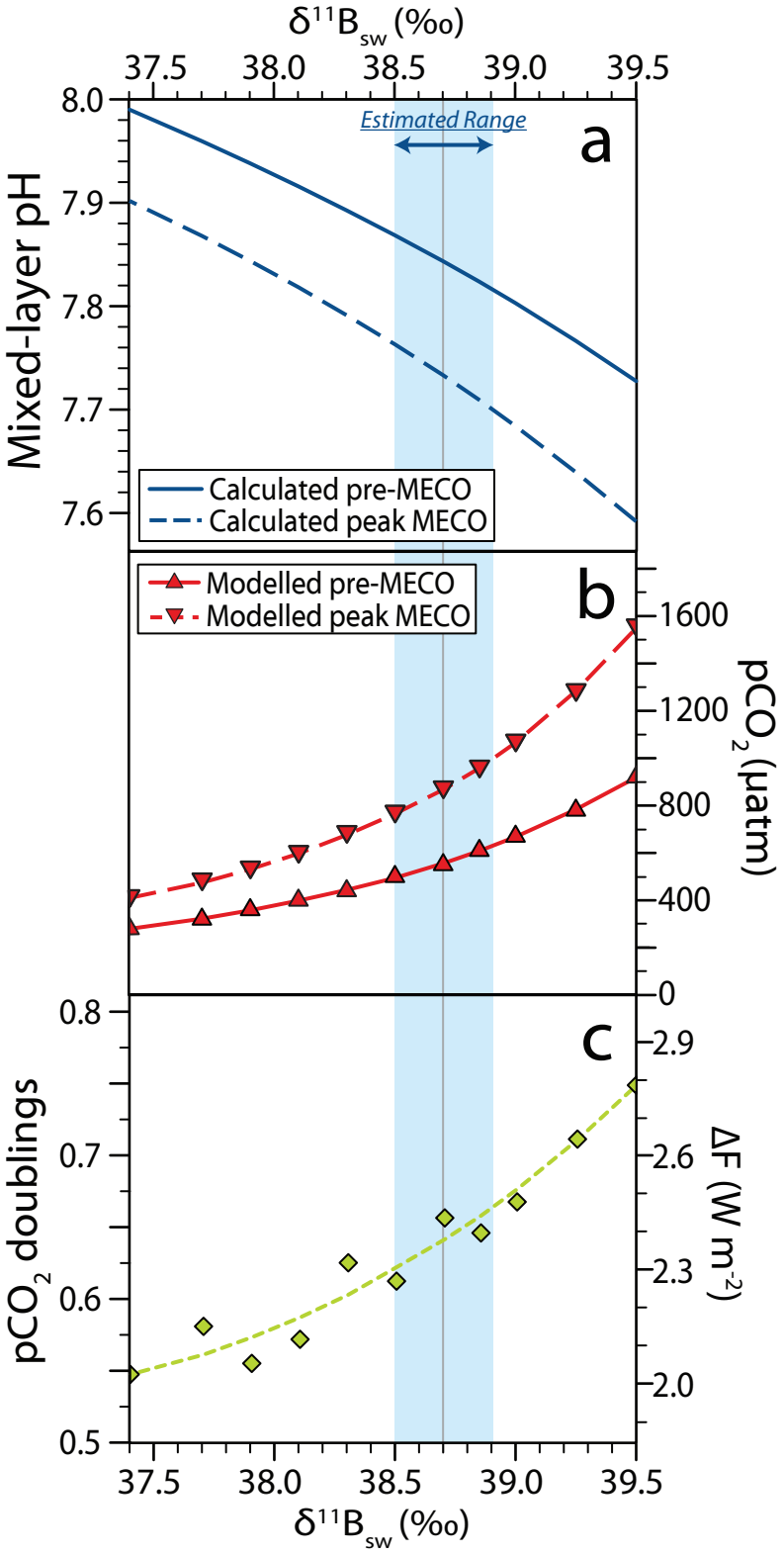
δ11Bsw (‰)
37.5
38.0
38.5
39.0
39.5
Estimated Range
a
Mixed-layer pH
8.0
7.9
7.8
7.7
7.6
Calculated pre-MECO
Calculated peak MECO
b
Modelled pre-MECO
Modelled peak MECO
pCO2 (µatm)
1600
1200
800
400
0
c
pCO2 doublings
0.8
0.7
0.6
0.5
ΔF (W m-2)
2.9
2.6
2.3
2.0
37.5
38.0
38.5
39.0
39.5
δ11Bsw (‰)

Figure 9.

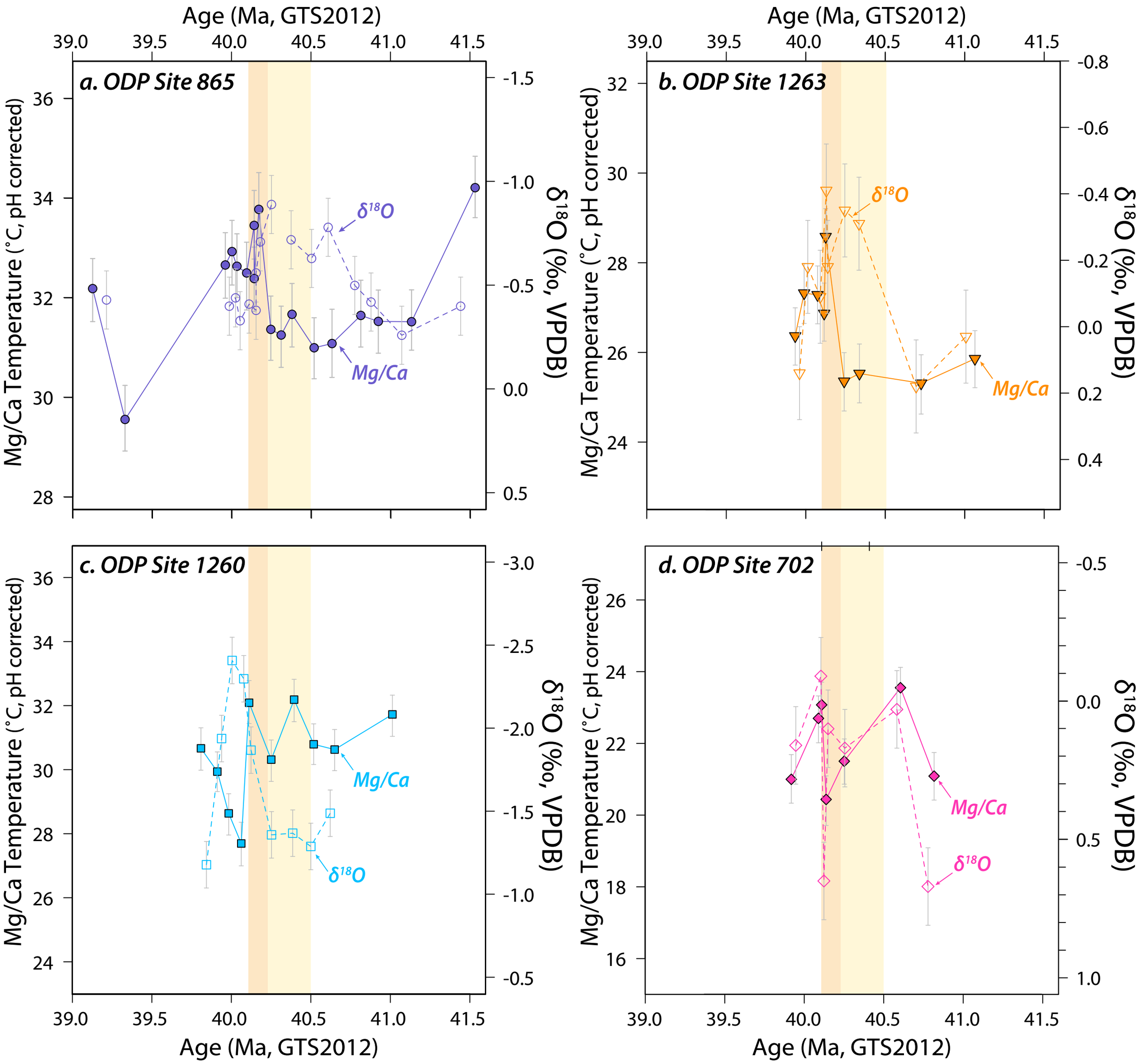
a. ODP Site 865
b. ODP Site 1263
c. ODP Site 1260
d. ODP Site 702
Age (Ma, GTS2012)
Mg/Ca Temperature (°C, pH corrected)
δ18O (‰, VPDB)
Mg/Ca
δ18O
39.0
39.5
40.0
40.5
41.0
41.5